2021-06-03

The Influence of Particle Concentration on the Formation of Settling-Driven Gravitational Instabilities at the Base of Volcanic Clouds

Fries, A

10.3389/feart.2021.640090
Frontiers in Earth Science
Frontiers Media

frontiers in Earth Science

ORIGINAL RESEARCH
published: 03 June 2021
doi: 10.3389/feart.2021.640090

The Influence of Particle Concentration on the Formation of Settling-Driven Gravitational Instabilities at the Base of Volcanic Clouds

Allan Fries[1], Jonathan Lemus[1,2], Paul A. Jarvis[1], Amanda B. Clarke[3,4], Jeremy C. Phillips[5], Irene Manzella[6] and Costanza Bonadonna[1]*

[1]Department of Earth Sciences, University of Geneva, Geneva, Switzerland, [2]Department of Computer Science, University of Geneva, Geneva, Switzerland, [3]School of Earth and Space Exploration, Arizona State University, Tempe, AZ, United States, [4]Istituto Nazionale di Geofisica e Vulcanologia, Sezione di Pisa, Pisa, Italy, [5]School of Earth Sciences, University of Bristol, Bristol, United Kingdom, [6]School of Geography, Earth and Environmental Sciences, University of Plymouth, Plymouth, United Kingdom

OPEN ACCESS

Edited by:
Stephen Self, University of California, Berkeley, United States

Reviewed by:
Thierry Menand, Université Clermont Auvergne, France
Larry Garver Mastin, United States Geological Survey (USGS), United States

***Correspondence:**
Allan Fries
allan.fries@unige.ch

Specialty section:
This article was submitted to Volcanology, a section of the journal Frontiers in Earth Science

Received: *10 December 2020*
Accepted: *07 May 2021*
Published: *03 June 2021*

Citation:
Fries A, Lemus J, Jarvis PA, Clarke AB, Phillips JC, Manzella I and Bonadonna C (2021) The Influence of Particle Concentration on the Formation of Settling-Driven Gravitational Instabilities at the Base of Volcanic Clouds. Front. Earth Sci. 9:640090. doi: 10.3389/feart.2021.640090

Settling-driven gravitational instabilities observed at the base of volcanic ash clouds have the potential to play a substantial role in volcanic ash sedimentation. They originate from a narrow, gravitationally unstable region called a Particle Boundary Layer (PBL) that forms at the lower cloud-atmosphere interface and generates downward-moving ash fingers that enhance the ash sedimentation rate. We use scaled laboratory experiments in combination with particle imaging and Planar Laser Induced Fluorescence (PLIF) techniques to investigate the effect of particle concentration on PBL and finger formation. Results show that, as particles settle across an initial density interface and are incorporated within the dense underlying fluid, the PBL grows below the interface as a narrow region of small excess density. This detaches upon reaching a critical thickness, that scales with $(\nu^2/g')^{1/3}$, where ν is the kinematic viscosity and g' is the reduced gravity of the PBL, leading to the formation of fingers. During this process, the fluid above and below the interface remains poorly mixed, with only small quantities of the upper fluid phase being injected through fingers. In addition, our measurements confirm previous findings over a wider set of initial conditions that show that both the number of fingers and their velocity increase with particle concentration. We also quantify how the vertical particle mass flux below the particle suspension evolves with time and with the particle concentration. Finally, we identify a dimensionless number that depends on the measurable cloud mass-loading and thickness, which can be used to assess the potential for settling-driven gravitational instabilities to form. Our results suggest that fingers from volcanic clouds characterised by high ash concentrations not only are more likely to develop, but they are also expected to form more quickly and propagate at higher velocities than fingers associated with ash-poor clouds.

Keywords: settling-driven gravitational instabilities, tephra sedimentation, volcanic ash clouds, ash concentration, analogue experiments, PLIF

INTRODUCTION

Many studies have highlighted that sedimentation from buoyant particle-laden currents (e.g., river plumes or volcanic ash clouds) is affected by collective settling mechanisms such as particle aggregation (Nicholas and Walling, 1996; Zimmermann-Timm, 2002; Costa et al., 2010; Durant and Brown, 2016) and settling-driven gravitational instabilities (Hoyal et al., 1999b; Parsons et al., 2001; Carazzo and Jellinek, 2012; Manzella et al., 2015). Both processes promote the scavenging of fine particles by increasing their fall velocities with respect to their individual settling rates. In particular, they can explain the fine-ash depletion observed in large volcanic clouds far from the source (Hoyal et al., 1999b; Carazzo and Jellinek, 2013; Durant, 2015; Gouhier et al., 2019). Many studies have already shown how particle aggregation can play a substantial role in enhancing fine ash sedimentation through the formation of clusters which might descend faster and closer to the vent than individual fine ash particles (Brown et al., 2012; Bagheri et al., 2016; Folch et al., 2016). However, less attention has been paid to settling-driven gravitational instabilities that can develop at the base of volcanic clouds and result in the formation of downward moving plumes, called ash fingers, within which fine ash particles fall faster than they do individually. Tephra dispersal and sedimentation can affect communities at multiple spatial and temporal scales (Jenkins et al., 2015; Bonadonna et al., 2021) including disruption to aviation (Guffanti et al., 2009; Prata and Tupper, 2009; Lechner et al., 2017), impact to public health (Horwell and Baxter, 2006; Gudmundsson, 2011) and damage to both residential buildings and critical infrastructures (Spence et al., 2005; Wilson et al., 2012). Therefore, understanding the processes controlling tephra sedimentation, including settling-driven gravitational instabilities, is fundamental for developing more efficient ash dispersal models and better managing the associated risk (Scollo et al., 2008; Folch, 2012; Durant, 2015).

Settling-driven gravitational instabilities develop at the base of particle suspensions from density differences generated by particles settling across the interface and their incorporation into the underlying fluid (**Figures 1A,B**). The configuration is an initially stable density stratification with a buoyant particle suspension (e.g., volcanic ash cloud) emplaced above a slightly denser fluid (e.g., atmosphere). The region immediately below the density interface becomes denser than the underlying layer when particles settle through it, forming a heavy, interfacial Particle Boundary Layer (PBL) (Burns and Meiburg, 2012; Burns and Meiburg, 2015; Yu et al., 2013; Davarpanah Jazi and Wells, 2020). Once the system is unstable, the PBL detaches and particle-laden bulbous plumes (called fingers) sink and protrude into the lower layer (Hoyal et al., 1999b). These fingers descend rapidly, driving particle sedimentation at faster velocities and rates than individual particle settling. In this paper, we refer to this finger-producing mechanism as settling-driven gravitational instabilities, where fingers are identified as the downward moving particle-laden plumes. We define the PBL as the heavy particle-laden layer formed below the initial density interface by the inclusion of particles in the dense underlying fluid.

Settling-driven gravitational instabilities can affect the sedimentation from buoyant flows that are associated with various natural systems including river (hypopycnal) plumes (Hoyal et al., 1999b; Maxworthy, 1999; Parsons et al., 2001; Henniger and Kleiser, 2012; Davarpanah Jazi and Wells, 2016; Sutherland et al., 2018; Davarpanah Jazi and Wells, 2020), magma

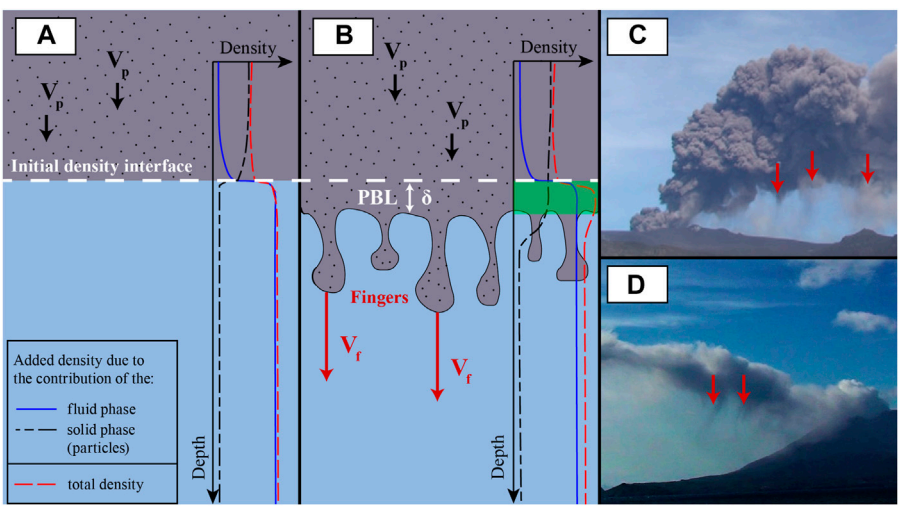

FIGURE 1 | Schematic representation of the mechanism by which settling-driven gravitational instabilities arise. **(A)** The particle suspension (gray) initially overlies particle-free fluid (blue) and the density profile is stable. **(B)** Particles settle at their individual fall velocity (V_p) across the density interface between the particle suspension and the underlying, initially denser lower fluid, forming a dense Particle Boundary Layer (PBL) of thickness δ, highlighted in green, that contains density contributions from both the solid and fluid phases. Destabilization of the density stratification leads to the formation of fingers that rapidly descend at a speed $V_f > V_p$. Ash fingers have been observed at the base of volcanic clouds including **(C)** Eyjafjallajökull 2010, Iceland (Manzella et al., 2015), and **(D)** Sakurajima 2019, Japan. Red arrows highlight the presence of fingers. Note that more complex mechanisms than pure individual settling such as wind-driven stirring can also affect the particle delivery to the PBL in these natural examples and modify the density configuration that gives rise to ash fingers.

chambers (Marsh, 1988), vertical tephra transport in oceans (Carey, 1997; Manville and Wilson, 2004; Jacobs et al., 2013; Jacobs et al., 2015) and volcanic clouds (Carazzo and Jellinek, 2012; Manzella et al., 2015; Scollo et al., 2017). Hence, several authors from different fields have investigated these instabilities through a combination of experiments, theoretical analyses and numerical simulations (Hoyal et al., 1999b; Cardoso and Zarrebini, 2001; Burns and Meiburg, 2012; Burns and Meiburg, 2015; Carazzo and Jellinek, 2012; Jacobs et al., 2013; Yu et al., 2013, 2014; Chou and Shao, 2016; Scollo et al., 2017). Whilst the instability mechanism here resembles the classical Rayleigh-Taylor instability which occurs when a dense fluid overlies a lighter one (Sharp, 1984; Linden and Redondo, 1991) the characteristics and dynamics differ in critical ways. A key difference is that this instability originates from the settling of particles out of the upper layer, forming a narrow region of excess density (the PBL). The interface between the upper layer and the PBL is gravitationally stable, which means that, unlike in classical Rayleigh-Taylor problems, the upper layer does not undergo overturning. Simultaneously, there is competition between the rate at which the PBL forms due to particle settling and the rate at which it is destroyed by gravitational instability within the lower layer. The finite-amplitude characteristics of the instability are therefore different.

In addition to particle settling, double diffusion, where two density-altering fluid properties diffuse at different rates, can also lead to the formation of an unstable interfacial region and associated fingers (Green, 1987; Chen, 1997; Hoyal et al., 1999a; Carazzo and Jellinek, 2013). A comparison between the diffusive and particle-settling fluxes allows differentiation between the two mechanisms (Green, 1987; Hoyal et al., 1999a; Carazzo and Jellinek, 2013); settling-driven gravitational instabilities can occur if the settling flux is greater than the diffusive flux. Both mechanisms are likely to coexist and to affect the sedimentation from volcanic clouds because of thermal diffusion and particle settling (Carazzo and Jellinek, 2013). However, in this paper, we focus on settling-driven gravitational instabilities which are more suitable for describing finger formation during the spreading of an ash cloud at neutral buoyancy, once it is thermally equilibrated with the atmosphere (Manzella et al., 2015; Scollo et al., 2017). As we will show in *Experimental configuration*, the particle flux into the PBL in our experiments is predominantly controlled by particle settling rather than double diffusion and we therefore only address gravitational instabilities arising because of particle settling across the interface.

Hoyal et al. (1999b) showed that the criterion for convection to start at the base of particle suspensions and for fingers to develop depends on the ratio between driving gravitational forces and resisting viscous forces as represented by the Grashof number

$$Gr = \frac{g'\delta^3}{\nu^2}, \quad (1)$$

where δ is the PBL thickness (**Figure 1B**), ν the kinematic viscosity, and $g' = g(\rho - \rho_a)/\rho_a$ the reduced gravity of the PBL, with $g = 9.81\ \mathrm{m\,s^{-2}}$ the acceleration due to gravity, and ρ and ρ_a the densities of the PBL and of the ambient, respectively (a list of symbols can be found in **Supplementary Table S1**). By analogy with thermal convection, Hoyal et al. (1999b) proposed that the instability starts above a critical Grashof number of the order of 10^3. For given values of the reduced gravity and viscosity, this indicates that fingers develop only if the PBL can grow to a critical thickness $\delta_c = 10\,(\nu^2/g')^{1/3}$. Their experimental measurements further revealed that the instability wavelength (i.e., the spacing between fingers) and the finger width are proportional to the critical PBL thickness.

Another condition for the development of fingers due to settling-driven gravitational instabilities is that the particle-fluid mixture behaves as a continuum (Hoyal et al., 1999b). The particle and fluid motions can then be coupled through terms in their respective momentum equations (Harlow and Amsden, 1975; Valentine and Wohletz, 1989; Burgisser et al., 2005). In dilute mixtures, such as fingers, the degree of coupling can be assessed by calculating the Stokes and Sedimentation dimensionless numbers that quantify the relative strength of the forces the fluid and particles exert on each other (Crowe et al., 2011). For fingers to form, the coupling must be sufficiently strong for the finger velocity to be greater than the particle velocity. Carazzo and Jellinek (2012) showed that this last condition is met in numerous volcanic ash clouds, and effectively reduces to a dependence on particle size, with fine ash particles (diameter $d < 100\ \mu\mathrm{m}$) promoting finger formation. In a series of aqueous analogue experiments with both glass beads and natural ash, Scollo et al. (2017) found that particle concentration and size exerted a major control on the instability and that no fingers formed for particle diameters greater than approximately 125 μm. Larger particles instead settled individually, sufficiently decoupled from the fluid phase. Finally, their experiments revealed that the ash composition did not significantly change finger dynamics, suggesting that, for a given ash size distribution, fingers can form underneath plumes regardless of the magma composition.

Ash fingers associated with settling-driven gravitational instabilities have been observed in various volcanic eruptions, e.g., Mount Redoubt, USA, 1990 (Hobbs et al., 1991); Ruapehu, New Zealand, 1996 (Bonadonna et al., 2005); Soufrière Hills, Montserrat, 1997 (Bonadonna et al., 2002); Eyjafjallajökull, Iceland, 2010 (Bonadonna et al., 2011; Manzella et al., 2015; **Figure 1C**); Etna, Italy, 2013 (Andronico et al., 2015; Scollo et al., 2017); and Sakurajima, Japan, 2019 (**Figure 1D**). Their association with different eruptive styles suggests that settling-driven gravitational instabilities are a common, widespread phenomenon.

Despite these observations, quantitative field descriptions of ash fingers remain rare. During the 2010 Eyjafjallajökull eruption, Manzella et al. (2015) found the average downward finger velocity to be about $1\ \mathrm{m\,s^{-1}}$, which is greater than the calculated settling velocities of individual ash particles finer than 100 μm ($V_p < 0.6\ \mathrm{ms^{-1}}$). They also characterised the geometry of the instability by showing that the width and spacing of individual fingers appeared to be similar, as suggested previously by experimental studies (Hoyal et al., 1999b; Carazzo and Jellinek, 2012). Scollo et al.

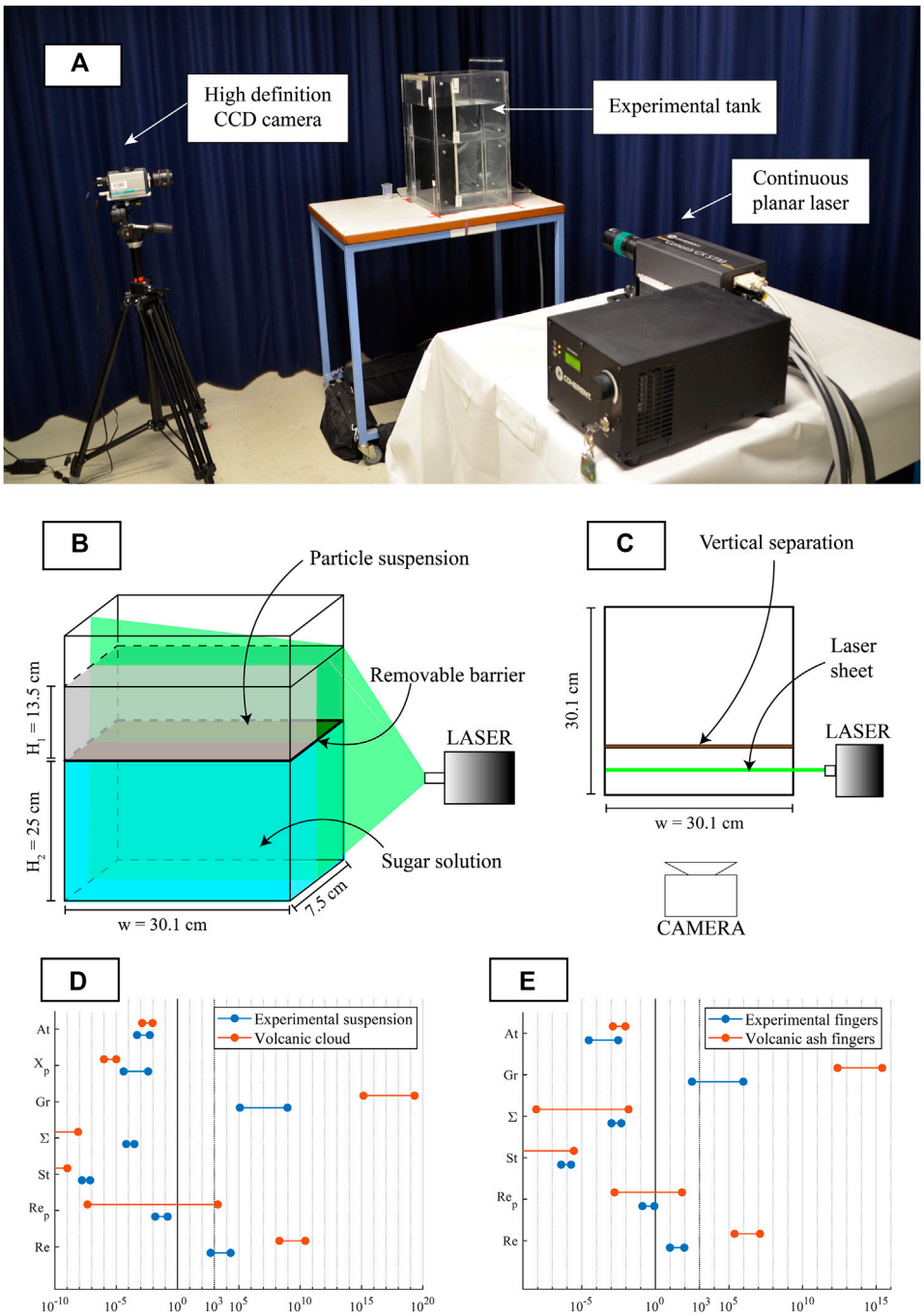

FIGURE 2 | (A) Experimental apparatus **(B)** Schematic of the tank configuration before barrier removal. The upper layer has a thickness H_1 that varies from 5 to 21 cm and is kept constant at 13.5 cm in type A experiments. In all experiments, the lower layer is a dense sugar solution with a thickness H_2 of 25 cm. The width of the tank w is 30.1 cm **(C)** Top view of the experimental configuration. The vertical separation and the laser plane are located 7.5 and 4.5 cm from the tank's front wall, respectively. **(D)** Comparison between experimental and natural dimensionless numbers (*Re*, Flow Reynolds number; Re_p, Particle Reynold number; *St*, Stokes number; Σ, Sedimentation number; *Gr*, Grashof number; X_p, Particle volume fraction; *At*, Atwood number) associated with ash clouds and **(E)** fingers. The vertical solid and dotted lines underline the values of 10^0 and 10^3 that are important for most dimensionless numbers.

(2017) suggested that Mass Eruption Rates (MERs) greater than about 10^5 kg s^{-1} favor the formation of settling-driven gravitational instabilities, which is in good agreement with analogue experiments where the particle concentration corresponds to highly concentrated volcanic clouds. Finally, using a combination of radar and disdrometer measurements at Stromboli, Italy, Freret-Lorgeril et al. (2020) detected intermittent periods of higher particle concentration that

they interpreted as fingers affecting the sedimentation from weak, short-lived plumes. Their work, along with recent experiments on particle-laden currents (Davarpanah Jazi and Wells, 2020), suggests that the wind and the relative motion of the current may affect the formation of ash fingers, evidencing that settling-driven gravitational instabilities are not the only mechanism by which ash fingers can be produced. However, in our experiments that are performed in the absence of relative horizontal motion between the particle suspension and the ambient fluid (that are initially separated by a flat interface), we only consider the case of volcanic ash clouds with negligible wind shear effects for which the particle flux across the interface is dominated by individual settling, i.e., where the plume and fingers are advected at wind speed at the neutral buoyancy level and far from the source.

While previous studies have built the theoretical framework to assess the conditions necessary for the formation of settling-driven gravitational instabilities and focused mainly on the effect of the particle size, which is of primary importance, we only have limited insights into the effect of the particle concentration on the formation of settling-driven gravitational instabilities. We present new experiments, performed over a wide range of initial conditions, to investigate the velocity and size of fingers at different particle concentrations and compare our results with existing models on settling-driven gravitational instabilities (Hoyal et al., 1999b; Carazzo and Jellinek, 2012; Manzella et al., 2015). Additionally, we explore the potential of particle suspensions to develop fingers by introducing a new dimensionless number relating the suspension and characteristic PBL thicknesses. Despite significant progress in theoretical (Burns and Meiburg, 2012) and numerical (Burns and Meiburg, 2015) studies of the formation of settling-driven gravitational instabilities, uncertainties remain regarding the density configuration associated with the triggering of the instabilities. Although the presence of a heavy PBL below the particle suspension is widely accepted, the composition of the fluid phase and the particle concentration in this region remain poorly-described, despite their importance for the bulk density of the suspension and the dynamics of the resulting fingers. We have used Planar Laser Induced Fluorescence (PLIF; Koochesfahani, 1984; Crimaldi, 2008) to measure the spatial and temporal evolution of the fluid phase density, specifically focusing on the PBL and fingers. Whilst previous experiments have focused on the particle concentration and velocity fields, our PLIF measurements allow for a complete characterisation of the density configuration associated with the triggering of the instability. Once developed, settling-driven gravitational instabilities are thought to significantly increase the sedimentation rate below particle suspensions. We quantify the particle mass flux in the experiments at different particle concentrations. Experimental findings are finally discussed in relation to the sedimentation of fine ash from volcanic ash clouds.

METHODS

Experimental Configuration

The experiments are performed in an experimental water tank $30.1 \times 30.1 \times 50.0\,\mathrm{cm}^3$ that is divided into two layers by a horizontal barrier (Manzella et al., 2015; Scollo et al., 2017; **Figure 2**; H_1 = 5–21 cm and H_2 = 25 cm are the thicknesses of the upper and the lower layers, respectively). Initially, the density profile is stable. The upper layer (ash cloud analogue) is a mixture of particles and fresh water, with initial particle concentrations C_u ranging from 0.0007 to $10\,\mathrm{g\,l^{-1}}$ (mixture density from 997 to $1{,}007\,\mathrm{kg\,m^{-3}}$), and the lower layer (atmosphere analogue) is a denser sugar solution kept at a constant density of $1{,}008\,\mathrm{kg\,m^{-3}}$ (sugar concentration of $29\,\mathrm{g\,l^{-1}}$). Experiments are performed at ambient temperature. This experimental configuration is inspired by the classical work of Hoyal et al. (1999b) on settling-driven gravitational instabilities and experiments on Rayleigh-Taylor instabilities (Linden and Redondo, 1991; Dalziel, 1993). This minimalist design allows us to study the effect of particle concentration on settling-driven gravitational instabilities and finger dynamics in isolation from other processes and variables.

The particles are spherical glass beads, which are suitable for modeling the behaviour of natural ash (Manzella et al., 2015; Scollo et al., 2017). They have a median diameter D_{50} of 41.5 μm and a sorting $\sigma = (D_{84} - D_{16})/2$ (Inman, 1952) of 14 μm (see **Supplementary Figure S1**), as measured by laser diffraction using a BetterSizer S3 Plus. The particle density is measured, using Helium pycnometery with a Ultrapyc 1200e, to be $2{,}519.2 \pm 0.1\,\mathrm{kg\,m^{-3}}$.

Particles are kept in suspension by continuously mixing the upper layer top to bottom for 20–25 s with an agitator composed of a $23 \times 7\,\mathrm{cm}^2$ millimetric mesh, that is large enough to mix the entire upper layer and produce homogeneous and repeatable mixing. Mixing is stopped 5 s before the experiment begins. The separation between the two layers is then removed manually by sliding the barrier out of its slot in 0.9–1.3 s. A major challenge of this experimental configuration is that mixing is generated across the density interface when removing the barrier and is clearly visible in the first 10 s of the experiments, affecting the early development of settling-driven gravitational instabilities. The perturbation is particularly strong near the back wall of the tank, so we reduced the length of the tank to 7.5 cm with rigid vertical separators to attenuate the effect of the vorticity (Manzella et al., 2015; Scollo et al., 2017). After barrier removal, particles start settling into the lower partition of the tank (see **Supplementary Video S1**). A continuous Nd:YAG planar laser (Genesis CX-SLM by Coherent) with a wavelength of 532 nm illuminates the experiments from the side of the tank and a sCMOS camera (HiSense Zyla by Dantec Dynamics), with 16 bit color depth, is used to capture images of the experiments at 10 Hz with image dimensions of $1{,}500 \times 2{,}100$ pixels, resulting in a resolution of $55\,\mathrm{px\,mm^{-1}}$. We find that the sugar concentration is sufficiently small that it has negligible effect on the light intensity received by the camera.

Gravitational instabilities in our setup can theoretically develop through two different mechanisms, double diffusion and particle settling (Hoyal et al., 1999a; Hoyal et al., 1999b; Burns and Meiburg, 2012). Double diffusive effects arise when two density-altering fluid properties (i.e., sugar and particles in the lower and the upper layers, respectively) diffuse at differential rates. The faster diffusion of one

TABLE 1 | Top - Typical dimensional parameter ranges for the variables used in the scaling analysis for both natural and experimental systems.

Parameter name (unit)	Symbol	Volcanic cloud	Experimental suspensions	Ash fingers	Experimental fingers
Characteristic velocity (m s^{-1})	V	50–150[c]	10^{-2}–10^{-1}	0.5–1.5[d]	5×10^{-3}–15×10^{-3}
Characteristic thickness (m)	L	1,200–3,900[b]	0.05–0.21	142–194[d]	8×10^{-3}–2.5×10^{-2}
Cloud thickness or finger width					
Gravitational acceleration (m s^{-2})	g	9.81	9.81	9.81	9.81
PBL thickness (m)	δ	70–100[d]	5×10^{-3}–10^{-2}	70–100[d]	5×10^{-3}–10^{-2}
PBL density (kg m^{-3})	ρ	0.1–1.32[d]	1,008–1,018	0.1–1.32[d]	1,008–1,018
Ambient density (kg m^{-3})	ρ_a	0.1–1.3[c,d]	1,008	0.1–1.3[c,d]	1,008
Fluid density (kg m^{-3})	ρ_f	0.1–1.3[c,d]	997	0.1–1.3[c,d]	997
Particle density (kg m^{-3})	ρ_p	750–2400[f]	2,519.2	750–2400[f]	2,519.2
Particle volume fraction	X_p	10^{-6}–10^{-5c}	4.10^{-5}–4.10^{-3}	—	—
Particle diameter (m)	d	10^{-6}–10^{-3c}	26×10^{-6}–57×10^{-6}	10^{-6}–10^{-3c}	26×10^{-6}–57×10^{-6}
Dynamic viscosity (Pa s^{-1})	μ	$3 \times 10^{-5c,f}$	10^{-3b-e}	$3 \times 10^{-5c,f}$	10^{-3b-e}
Kinematic viscosity	ν	3×10^{-5a}	10^{-6b}	3×10^{-5a}	10^{-6b}
Characteristic velocity fluctuations (m s^{-1})	ΔU	2.5[b]	10^{-3}	0.125[b]	4×10^{-3}
Characteristic fluctuation lengthscale (m)	δ_f	120[b]	0.135	14[b]	8×10^{-3}
Stokes drag correction	k_S	1–2.5[g]	1[g]	1–2.5[g]	1[g]
Newton drag correction	k_N	1–10^{3g}	1[g]	1–10^{3g}	1[g]

Dimensionless numbers	Formula	Volcanic cloud	Experimental suspensions	Ash fingers	Experimental fingers
Reynolds (Re)[e]	$\frac{\rho VL}{\mu}$	10^8 – 10^{10}	10^2 – 10^4	10^5 – 10^7	10^1 – 10^2
Particle Reynolds (Re_p)[c,e]	$\frac{\rho_f V_p d}{\mu}$	10^{-8} – 10^3	10^{-2} – 10^{-1}	10^{-3} – 10^2	10^{-1} – 10^0
Stokes (St)[a]	$\frac{(\rho_p-\rho_f)d^2}{18\mu f}\left(\frac{\Delta U}{\delta_f}\right)\left(1+\frac{\rho_f}{2\rho_p}\right)$	10^{-16} – 10^{-9}	10^{-8} – 10^{-7}	10^{-13} – 10^{-6}	10^{-7} – 10^{-6}
Sedimentation (Σ)[a]	$\frac{(\rho_p-\rho_f)d^2}{18\mu f}\left(\frac{g}{\Delta U}\right)$	10^{-15} – 10^{-8}	10^{-5} – 10^{-4}	10^{-9} – 10^{-2}	10^{-3} – 10^{-2}
Grashof (Gr)[f]	$\frac{g'\delta^3}{\nu^2}$	10^{15} – 10^{19}	10^5 – 10^8	10^{12} – 10^{15}	10^2 – 10^6
Atwood (At)[d]	$\frac{\rho-\rho_a}{\rho+\rho_a}$	10^{-3} – 10^{-2}	10^{-3} – 10^{-2}	10^{-3} – 10^{-2}	10^{-5} – 10^{-3}

Top - Typical dimensional parameter ranges for the variables used in the scaling analysis for both natural and experimental systems. Bottom - Dimensionless numbers associated with natural processes and experiments. Note that parameters associated with volcanic clouds (e.g. cloud thickness) can stray beyond the typical ranges given (Suzuki and Koyaguchi, 2009; Ansmann et al., 2010). Distinct values were considered for the particle-laden layer (volcanic ash cloud or particle suspension) and for the fingers.

[a] *Burgisser and Bergantz (2002).*
[b] *Burgisser et al. (2005).*
[c] *Carazzo and Jellinek (2012).*
[d] *Manzella et al. (2015).*
[e] *Kavanagh et al. (2018).*
[f] *Roche and Carazzo (2019).*
[g] *Bagheri and Bonadonna (2016a).*

component relative to the other can lead to a local increase of the bulk density at the interface that triggers gravitational instabilities. The rate at which the bulk density increases in double-diffusive systems is therefore controlled by the diffusion of the fastest diffusing component. Conversely, settling-driven gravitational instabilities are generated by particles settling across the interface, causing the upper part of the lower layer (i.e., the PBL) to become heavier than the fluid below. Gravitational instabilities produced by particle settling are therefore controlled by both the vertical velocity of the particles and the initial particle concentration of the upper layer. We determine the mechanism that provokes the formation of instabilities in our experiments by calculating the ratio of the double diffusive and settling fluxes, F_D and F_I, respectively, at the density interface (Green, 1987; Hoyal et al., 1999a; Carazzo and Jellinek, 2013)

$$F^* = \frac{F_D}{F_I}. \tag{2}$$

Replacing the fluxes by their expressions $F_D = \frac{1}{20}\rho_u (g\kappa_f \beta_m)^{\frac{1}{3}} (C_u/\rho_p)^{\frac{4}{3}}$ and $F_I = C_u g d^2 (\rho_p - \rho_f)/18\mu$ (Hoyal et al., 1999a; Carazzo and Jellinek, 2013), where κ_f is the diffusion coefficient of the fastest diffusing substance, μ the dynamic viscosity of the fluid, C_u the initial particle concentration in the upper layer (in mass per unit volume), ρ_p the particle density, d the particle diameter, $\beta_m \sim (\rho_p - \rho_f)/\rho_p$ the volumetric expansion coefficient of a particle suspension and ρ_u and ρ_f the density of the particle suspension and of the fluid phase, respectively, **Eq. 2** can be written as

$$F^* \approx \frac{9\mu\rho_u\left(\kappa_f\beta_m C_u\right)^{\frac{1}{3}}}{10d^2\left(\rho_p-\rho_f\right)\left(\rho_p^2 g\right)^{\frac{2}{3}}}. \tag{3}$$

$F^* >> 1$ means that double diffusion dominates the mass flux across the interface, whilst particle settling dominates for $F^* << 1$. In our experiment, the particles are the fastest diffusing substance, with a maximum hydrodynamic diffusion

coefficient κ_p of 1.2×10^{-7} m^2 s^{-1} (Lee et al., 1992; Martin et al., 1994). We find that F^* is between 8×10^{-4} and 2×10^{-2} in our experiments, suggesting that settling is the principal mechanism provoking the formation of fingers, with a negligible contribution of double diffusive effects.

Scaling of Experiments

Our experiments are dedicated to correctly reproducing the processes affecting ash sedimentation beneath volcanic clouds in a small, simplified configuration. The difference in complexity and scale between the natural phenomenon and small-scale experiments raises the problem of the applicability of the analogue experimental results. To address this, we perform a scaling analysis (Burgisser and Bergantz, 2002; Burgisser et al., 2005; Carazzo and Jellinek, 2012; Kavanagh et al., 2018; Roche and Carazzo, 2019). Dimensionless numbers relevant to our problem are calculated for volcanic ash clouds and compared with particle suspensions (**Figure 2D**). We also compare the dynamical regimes of natural ash and experimental fingers based on dimensionless numbers (**Figure 2E**). The values of the parameters associated with volcanic clouds and fingers are obtained from the literature (**Table 1**; Burgisser et al., 2005; Carazzo and Jellinek, 2012; Manzella et al., 2015).

The Reynolds number $Re = \rho VL/\mu$, with μ the fluid dynamic viscosity and V and L the characteristic velocity and length scale of the flow, respectively, characterises the flow behavior by comparing the inertial to viscous forces in the fluid. Re is greater in natural volcanic clouds and fingers, where it is far above the mixing transition (Re > 1,000–4,000) and is fully turbulent. Hence, we can expect particle collisions and entrainment of the ambient fluid to be enhanced in natural ash fingers, compared with their experimental counterparts. However, the flows in both experiments and volcanic clouds are inertia-controlled, suggesting that they are comparable despite the fact that velocity fluctuations (i.e., turbulence) are greater in natural flows.

In situations involving particle settling in fluids, the particle Reynolds number $Re_p = \rho_f V_p d/\mu$ is used to assess the properties of the flow surrounding particles and the subsequent drag force acting on them. d is the particle diameter and V_p is the individual particle settling velocity given by the Stokes terminal velocity in the experiments

$$V_p = \frac{gd^2\left(\rho_p - \rho_f\right)}{18\rho_f \nu}. \tag{4}$$

At subcritical $Re_p < 3 \times 10^5$, the drag factor f, which assesses the importance of the fluid resistance exerted on the particles, can be expressed as a function of Re_p and two drag correction coefficients depending on the particle shape k_N and k_S by Bagheri and Bonadonna (2016a), Bagheri and Bonadonna (2016b)

$$f = \frac{24k_S}{Re_p}\left[1 + 0.125\left(Re_p k_N / k_S\right)^{\frac{2}{3}}\right] + \frac{0.46k_N}{1 + \frac{5330}{Re_p k_N / k_S}}. \tag{5}$$

For multiphase flows involving particles, the Stokes St and Sedimentation Σ numbers quantify the momentum transfer between the fluid phase and the particles (Burgisser et al., 2005; Roche and Carazzo, 2019). They are calculated as

$$St = \frac{\left(\rho_p - \rho_f\right)d^2}{18\mu f}\left(\frac{\Delta U}{\delta_f}\right)\left(1 + \frac{\rho_f}{2\rho_p}\right), \tag{6}$$

and

$$\Sigma = \frac{\left(\rho_p - \rho_f\right)d^2}{18\mu f}\left(\frac{g}{\Delta U}\right) = \frac{V_p}{\Delta U}, \tag{7}$$

with ΔU the characteristic velocity fluctuation over a characteristic distance δ_f. These two parameters allow us to assess the coupling between particles and fluid. When $St << 1$ and $\Sigma << 1$, particles are strongly coupled with the fluid. This is the case for both natural ash and experimental fingers, satisfying the assumption that particles remain coupled with the fluid for fingers to form (Hoyal et al., 1999b; Carazzo and Jellinek, 2012).

Previous studies have invoked a convective mechanism for finger formation whose initiation depends on the Grashof number Gr, which can be estimated using a combination of experimental and field observations (see section *Finger Length Scales in Experiments: PBL Thickness, Finger Width and Finger Spacing*). Our analysis shows that Gr is much greater in the natural systems than in the experiments but that, in both configurations, it exceeds the critical Grashof number $Gr_c = 10^3$ (Hoyal et al., 1999b) for the development of settling-driven gravitational instabilities.

For scaling the density ratio between the particle-laden layer and the underlying fluid, we calculate the Atwood number $At = (\rho - \rho_a)/(\rho + \rho_a)$. At is commonly used to parameterise the density difference between two fluid layers, notably in experiments on Rayleigh-Taylor instabilities (Dalziel, 1993; Wilson and Andrews, 2002). Here, $At << 1$ in all configurations, showing that the difference in density between the two layers is very small in nature as well as in experiments and that the instability develops from small initial density differences in both situations.

For settling-driven gravitational instabilities, the natural and experimental ranges of Re_p, At, St and Σ all overlap while they are different for Re and Gr, but above critical threshold values that ensure that experiments are comparable to the volcanic phenomenon. We also note that the dimensionless numbers systematically cover a wider range in nature than in experiments (**Table 1**). This can firstly be explained by the wide variety of eruptive source and atmospheric conditions which means eruptive clouds can be associated with a wide range of particle diameters, characteristic velocities and length scales. Moreover, a second explanation is that descriptions of ash fingers remain rare, meaning they are currently poorly constrained, with high associated uncertainties. Altogether, this scaling analysis shows that our experiments do a good job reproducing most dimensionless numbers associated with natural clouds and fingers, although the variability of natural phenomena means that they are associated with larger ranges of Re and Gr, potentially extending to greater values than in our experiments. However, it is inevitable that laboratory models of

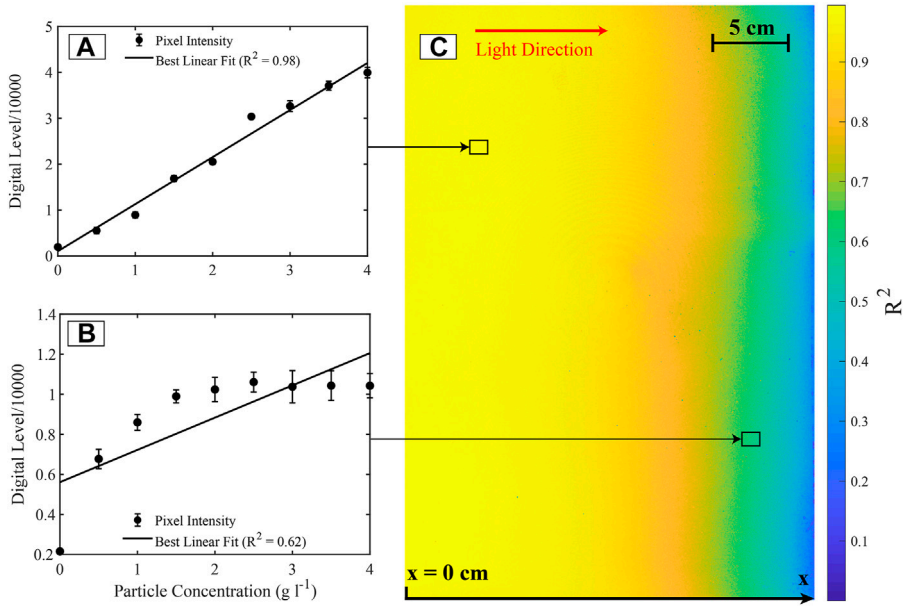

FIGURE 3 | Calibration of the particle concentration for a laser power of 0.50 W. **(A)** Example of a linear relationship between particle concentration and the light intensity in one pixel. In this example, the coefficient of determination R^2 suggests a very good linear fit. **(B)** Example of a pixel with a low-quality linear regression. Vertical error bars in panels A and C represent the standard deviation of the averaged pixel digital level over 10 s. **(C)** Map of R^2 inside the tank. R^2 diminishes as a function of x (distance from the wall closest to the laser).

volcanic clouds cannot capture the full range of variability of the natural system (Carazzo and Jellinek, 2012; Kavanagh et al., 2018; Roche and Carazzo, 2019). Despite this, given that that the ranges of *Re* and *Gr* in both the experiments and natural clouds are close to or above expected transitional values (Reynolds, 1883; Hoyal et al., 1999b), we can regard our experiments as suitable analogues to study settling-driven gravitational instabilities at the base of volcanic clouds.

Imaging Techniques

In order to independently obtain both the particle concentration C and fluid density fields, we imaged the particles using a set-up derived from Particle Image Velocimetry (PIV; Keane and Adrian, 1992; Grant, 1997; Adrian, 2005), and the fluid phase using Planar Laser Induced Fluorescence (PLIF; Koochesfahani, 1984; Crimaldi, 2008), in separate repeated experiments. These two techniques have previously been applied separately or simultaneously (Borg et al., 2001; Hu et al., 2002) to assess the particle concentration and velocity fields, as well as fluid properties such as temperature and density, in other aqueous experiments. Here we apply particle imaging and PLIF on separate experiments where we kept the experimental set-up in the same configuration, including identical starting conditions, i.e., particle size and concentration and fluid density contrast, as well as identical imaging conditions, i.e., camera and laser positions and settings. Ensuring the same experimental and imaging conditions is critical in order to enable the combination of the results given by the two techniques (Borg et al., 2001). Moreover, we ensured that results from PLIF experiments were reproducible before combining with results from particle-imaging experiments (**Supplementary Figure S2**).

Particle Imaging

We developed a calibration that links the particle concentration C to the light intensity scattered by particles and received by the camera sensor, with the assumption that the light intensity observed in the experiments is linearly related to the particle concentration. During calibrations, the water tank is first filled with a fluid of uniform and known particle concentration (ranging from 0 to 6 g l^{-1} at 0.5 g l^{-1} concentration steps). The tank is then illuminated with different laser powers of 0.50, 0.45, 0.40, and 0.35 W for each particle concentration. In order to erase short temporal variations in particle concentration, calibration images are acquired at 0.1 s intervals and then averaged over 10 s. Finally, we perform an individual pixel-by-pixel calibration relating pixel intensity to particle concentration for each laser power. The pixel digital level (i.e., received light intensity) is positively linearly correlated with the particle concentration and the coefficient of determination is high, R^2 = 0.95 (**Figure 3A**). However, the light intensity through the width of the experimental tank is dependent on the particle concentration and exponentially attenuates with x, the distance from the tank wall closest to the laser. Hence, the quality of the linear regression between light intensity and particle concentration diminishes with distance from the light source (**Figures 3B,C**). For accurate particle concentration measurements, we therefore calculate concentration only in pixels with a coefficient of determination R^2 > 0.95. This corresponds to the pixels located in the 12 cm of the tank closest to the laser, limiting

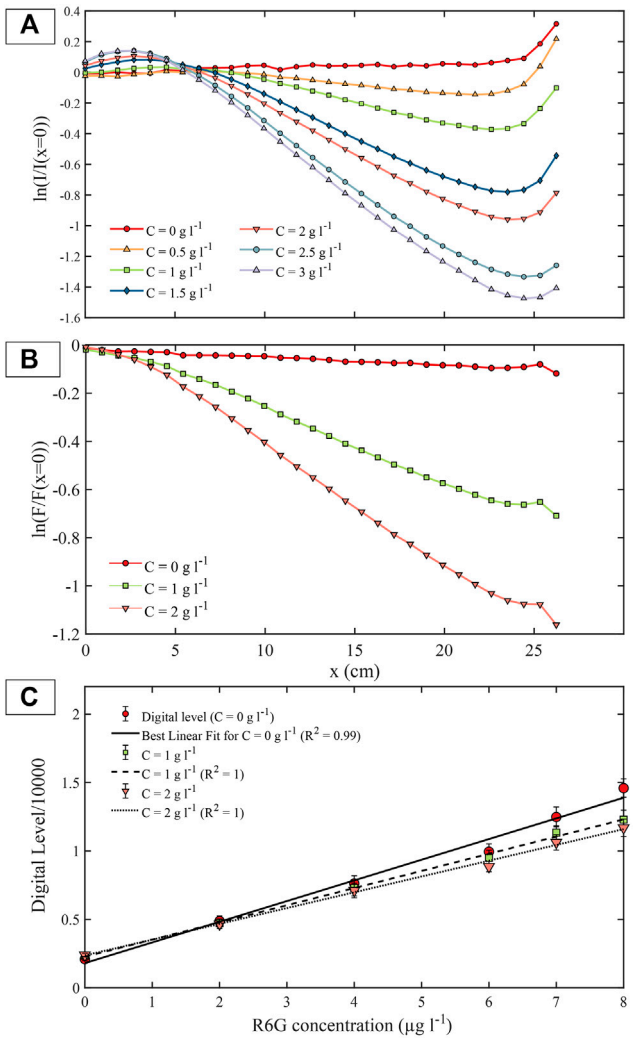

FIGURE 4 | (A) Profile of light intensity *I* as a function of distance from the laser source *x* (*x* = 0 corresponds to tank wall closest to laser) for different particle concentrations (without R6G). **(B)** Decrease of fluorescence intensity *F* for selected particle concentrations in PLIF calibrations. Note that, in both **(A,B)**, intensity is expressed as a logarithm normalized with its value at *x* = 0. **(C)** Example of Linear relations between R6G concentration and pixel digital level at different particle concentrations for a given pixel. The fluorescence intensity received by the camera diminishes with particle concentration, modifying the slope *p*. Vertical error bars in panels **A** and **C** represent the standard deviation of the averaged pixel digital level over 10 s.

the particle concentration measurements to approximately one third of the tank width. We assume that finger characteristics in this section are representative of those throughout the whole tank. Particle concentration measurements have already been employed to characterize settling-driven gravitational instabilities by Hoyal et al. (1999b) and Manzella et al. (2015). In both studies, the authors placed light sources behind or beside their experimental tanks and related light attenuation to the depth-averaged particle concentration in interrogation areas. With the present particle imaging scheme, we managed to improve the resolution of the concentration measurements down to the pixel-scale, which corresponds to a resolution of 0.18 mm in the horizontal and vertical directions. Furthermore, our measurements within the laser plane differ from depth-averaged particle concentration measurements and offer a visualization of the 2D particle concentration. We compare our particle concentration measurements obtained using this novel calibration procedure against those of Manzella et al. (2015). The two measurement techniques are in good qualitative agreement (**Supplementary Figure S3**). It is worth noting that whilst particle concentration measurements in the lower layer, into which the laser light enters directly, are highly accurate, corresponding measurements in the upper layer are affected by the refractive index change between the sugar solution and the particle suspension.

Fluid Phase Imaging

Understanding the behavior of the fluid phase associated with the occurrence of settling-driven gravitational instabilities is crucial to improving our general comprehension of the mechanisms driving the instability. In particular, it is important to quantify the contribution of the fluid phase on the generation of an unstable density profile associated with settling-driven gravitational instabilities. For this purpose, we applied the PLIF technique to a series of separate experiments. The PLIF approach yields quantitative, non-intrusive, measurements of fluid concentrations at high resolution (Koochesfahani, 1984; Crimaldi, 2008). It involves using a dye that generates fluorescence with an intensity linearly proportional to its concentration *D* when illuminated by a laser. In experiments on fluid mixing, by adding dye to one endmember, the fluorescence intensity can be used as a tracer, with the fluorescent dye concentration related to the proportion of dyed fluid (Linden and Redondo, 1991; Troy and Koseff, 2005; Dossmann et al., 2016). In the case presented here, mixing occurs between fluids of different density. The bulk density of the fluid phase thus changes during mixing and is quantified by the fluorescent dye concentration.

During our PLIF experiments, the upper layer is doped with Rhodamine 6G (R6G), a fluorescent dye with an absorption peak at 530 nm (Zehentbauer et al., 2014), close to the laser wavelength (532 nm), for a maximum absorption efficiency. The emission spectrum of R6G ranges from 510 to 710 nm with a peak at 560–580 nm, depending on the solvent (Zehentbauer et al., 2014). We isolate the R6G fluorescence from other light sources with a smaller wavelength (i.e., primary laser emission, particle scattering) by equipping the camera with a high-pass filter at 570 nm. This procedure allows us to image the R6G distribution only, as a proxy for the concentration of the upper fluid phase.

We perform a calibration in order to relate the local R6G dye concentration *D* to the digital level of individual pixels (i.e., fluorescence intensity). In PLIF measurements, the digital level *F* increases linearly with the R6G dye concentration *D* (Borg et al., 2001; Crimaldi, 2008)

$$F = (\phi \epsilon Pa(r,\theta)\gamma(r,\theta)\Delta A)D + R, \quad (8)$$

TABLE 2 | List of experiments.

Exp. Number	C (g l^{-1})	X_p	H_1 (cm)	L^*	Sedim	Number of repeats	Imaging techniques
Type A experiments							
A1	1	4.0×10^{-4}	13.5	11.3	F	3	particle imaging
A2	2	8.0×10^{-4}	13.5	14.2	F	3	particle imaging
A3	3	1.2×10^{-3}	13.5	16.3	F	4	particle imaging
A4	4	1.6×10^{-3}	13.5	17.9	F	3	particle imaging
A5	5	2.0×10^{-3}	13.5	19.3	F	3	particle imaging
A6	6	2.4×10^{-3}	13.5	20.5	F	3	particle imaging
A7	7	2.8×10^{-3}	13.5	21.6	F	3	particle imaging
A8	8	3.2×10^{-3}	13.5	22.6	F	3	particle imaging
A9	9	3.6×10^{-3}	13.5	23.5	F	3	particle imaging
A10	10	4.0×10^{-3}	13.5	24.3	F	3	particle imaging
A11	1	4.0×10^{-4}	13.5	11.3	F	3	PLIF
A12	2	8.0×10^{-4}	13.5	14.2	F	3	PLIF
Type B experiments							
B1	0.0007	2.8×10^{-7}	13.5	1.0	IPS	1	particle imaging
B2	0.001	4.0×10^{-7}	21	1.8	IPS	1	particle imaging
B3	0.0056	2.2×10^{-6}	13.5	2.0	IPS	1	particle imaging
B4	0.009	3.6×10^{-6}	5	0.8	IPS	1	particle imaging
B5	0.018	7.5×10^{-6}	13.5	3.0	IPS	1	particle imaging
B6	0.02	8.0×10^{-6}	21	4.8	F	1	particle imaging
B7	0.02	8.0×10^{-6}	17	3.8	IPS	1	particle imaging
B8	0.045	1.8×10^{-5}	13.5	4.0	IPS	2	particle imaging
B9	0.05	2.0×10^{-5}	7.5	2.3	IPS	1	particle imaging
B10	0.05	2.0×10^{-5}	10	3.1	IPS	1	particle imaging
B11	0.05	2.0×10^{-5}	17	5.2	F	1	particle imaging
B12	0.05	2.0×10^{-5}	21	6.5	F	1	particle imaging
B13	0.087	3.5×10^{-5}	13.5	5.0	F	2	particle imaging
B14	0.1	4.0×10^{-5}	5	1.9	IPS	1	particle imaging
B15	0.1	4.0×10^{-5}	7.5	2.9	IPS	1	particle imaging
B16	0.1	4.0×10^{-5}	10	3.9	IPS	1	particle imaging
B17	0.1	4.0×10^{-5}	17	6.6	F	1	particle imaging
B18	0.1	4.0×10^{-5}	21	8.1	F	1	particle imaging
B19	0.15	6.0×10^{-5}	5	2.2	F	1	particle imaging
B20	0.15	6.0×10^{-5}	7.5	3.3	F	1	particle imaging
B21	0.15	6.0×10^{-5}	13.5	6.0	F	1	particle imaging
B22	0.25	1.0×10^{-4}	5	2.6	F	1	particle imaging
B23	0.25	1.0×10^{-4}	7.5	3.9	F	1	particle imaging
B24	0.25	1.0×10^{-4}	10	5.3	F	1	particle imaging
B25	0.36	1.4×10^{-4}	13.5	8.0	F	1	particle imaging
B26	0.5	2.0×10^{-4}	7.5	5.0	F	1	particle imaging
B27	0.5	2.0×10^{-4}	10	6.6	F	1	particle imaging
B28	1	4.0×10^{-4}	10	8.4	F	1	particle imaging
B29	3	1.2×10^{-3}	7.5	25	F	1	particle imaging
B30	3	1.2×10^{-3}	21	9.0	F	1	particle imaging

All experiments are performed with spherical glass beads, with a median diameter of 41.5 μm, and a lower layer density of 1,008 kg m^{-3}. Particle concentrations C and equivalent particle volume fractions X_p refer to the initial particle concentration in the upper layer. H_1 is the upper layer thickness and L a dimensionless number introduced in the section* Potential to Form Settling-Driven Gravitational Instabilities (***Eq. 17***)*. In the "Sedim." column, we indicate the presence of fingers by "F" whereas their absence (i.e., individual particle settling) is signaled by "IPS."*

in which ΔA is the pixel area, $a(r,\theta)$ the attenuation along the path, ϵ the dye absorption coefficient, P the laser power, ϕ the dye quantum efficiency, $\gamma(r,\theta)$ the spatial intensity distribution, R the residual light not related to R6G fluorescence, and r and θ the radial and the angular components, respectively, of the 2D polar coordinates describing the position of points within the laser plane. Keeping the same particle concentration, fluorescent dye, laser properties, camera settings and experimental configuration in all calibrations and experiments, ΔA, $a(r,\theta)$, P, ϕ, ϵ, $\gamma(r,\theta)$ and R can reasonably be assumed to be constant. **Equation 8** thus reduces to

$$F = pD + R\,, \tag{9}$$

where p and R are constants that can be determined by linear regression between F and D.

However, changing the particle concentration modifies the spatial intensity distribution because the particles have an attenuation effect on $a(r,\theta)$ and, therefore, the determination of p. In fact, complex optical effects including light scattering and shadowing take place in the presence of particles and the light intensity I decreases following approximately exponential curves, whose slope steepens with particle concentration (**Figure 4A**). Hence, in

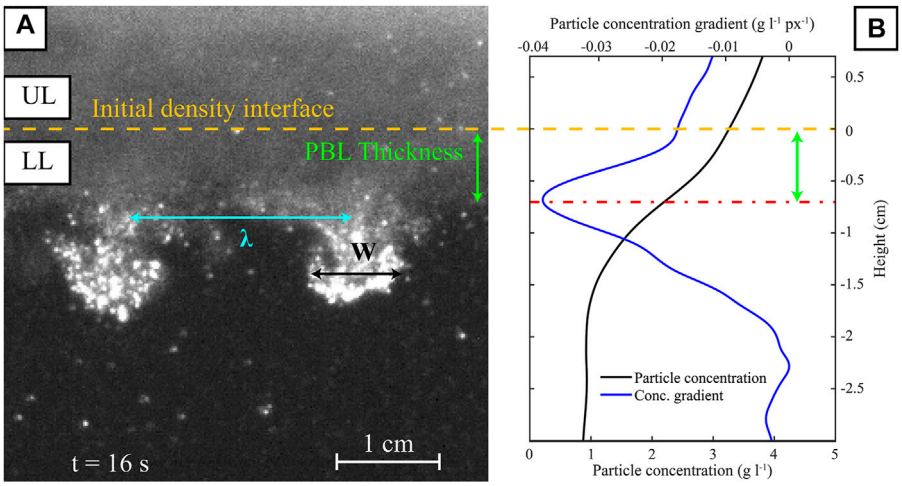

FIGURE 5 | (A) Visualization of fingers' geometrical properties for experiment A5 (5 g l^{-1}) 16 s after removing the barrier. The yellow dashed line is located at the position of the initial density interface and separates the Upper Layer (UL) and the Lower Layer (LL). Green, black and blue arrows indicate the PBL thickness and finger width (W) and spacing (λ), respectively. **(B)** Variation in the particle concentration (black line) and its gradient (blue line) with height, in the region across the density interface 16 s after barrier removal. The lower boundary of the PBL is identified at the level where the particle concentration gradient reaches its minimum value (represented by the dotted red line).

order to study the mixing between a particle-laden and a clear fluid, it is necessary to account for this effect (Borg et al., 2001). Whilst calibrations are performed with a uniform particle concentration, the spatial distribution of particles in the experiments can be very complex. Therefore, since the particle and R6G concentrations cannot be assessed simultaneously in this experimental set-up, we conduct PLIF calibrations using different particle concentrations. The difference between calibrations allows us to assess the uncertainty on measurements where the particle concentration is unknown. To obtain minimum uncertainties, we perform calibrations for particle concentrations of 0, 1, and 2 g l^{-1}, where the light intensity diminishes to a minimum of 33% of its initial value (**Figure 4A**). The effect of particle concentration on R6G fluorescence through the width of the tank is shown in **Figure 4B**. It is clear that small particle concentration differences can drastically reduce the intensity of fluorescence by attenuating the spatial light distribution inside the tank.

We conduct PLIF calibrations varying the particle and R6G concentration whilst keeping a constant laser power of 1.15 W. The water tank is filled with a uniform dye concentration ranging from 0 to 8 μg l^{-1} for three particle concentrations: 0, 1, and 2 g l^{-1}. Calibration images are averaged over 10 s in order to erase short temporal variations in fluorescence intensity. For each pixel, we fit the digital level and the R6G concentration to **Eq. 8** to determine p and R. In contrast with the particle concentration calibrations, the quality of the linear regression is good throughout the tank for a uniform particle concentration, where $a(r, \theta)$ is constant. However, the slope p is affected by the presence of particles as the fluorescence intensity diminishes with increasing particle concentration (**Figure 4C**), yielding an uncertainty on the measurements of R6G concentration and ultimately on the fluid density measurements. In the region of particular interest where the PBL forms, located within the first 5 cm below the barrier, we estimate the average uncertainty of the final fluid density measurement to be 0.1 and 0.8 kg m^{-3} for 1 and 2 g l^{-1} PLIF experiments, respectively (**Supplementary Figure S4**).

Experimental Conditions

We performed two types of experiments, with different objectives. Type A experiments are each repeated at least three times with the aim of separately characterising the fingers at different particle concentrations, and the density of the fluid phase (**Table 2**). In the first subset of type A experiments (A1–A10), we image the particles and vary the particle concentration from 1 to 10 g l^{-1}. In the second subset of type A experiments (A11–12), we repeat the same experiments but instead measure fluid phase properties using the PLIF technique, only with particle concentrations of 1 and 2 g l^{-1}. Type A experiments have a constant upper layer thickness of 13.5 cm and are imaged for 90 to 120 s after barrier removal.

In type B experiments, we explore the conditions that favor the formation of settling-driven gravitational instabilities by varying both the upper layer thickness (from 5 to 21 cm) and the particle concentration (from 7×10^{-4} to 3 g l^{-1}; **Table 2**). The maximum upper layer thickness is limited to 21 cm by the size of the water tank and we select the minimum thickness to be 5 cm in order to keep the upper layer much greater than the size of perturbations that could be induced by barrier removal. All type B experiments are particle-imaging experiments used to identify the presence or absence of settling-driven gravitational instabilities and are imaged for at least 180 s after barrier removal.

TABLE 3 | Summary of the measurements performed in type A experiments.

Parameter	Measurement	Method
PBL thickness δ	0.14–1.25 cm	Detection of the PBL thickness from analysis of the vertical particle concentration gradient
Finger width W	0.98–2.23 cm	Manual measurement of the width at finger's thickest point
Finger spacing λ	1.18–3.63 cm	Manual measurement of the distance separating adjacent fingers (at the level of the interface)
Maximum number of finger n	7–18	Detection of peaks in the digital level below the interface
Finger velocity V_f	0.34–1.38 cm s^{-1}	Manual tracking of the position of the finger front
Particle concentration in the PBL	0.8–9 g l^{-1}	Linear relation between the camera digital level and the particle concentration
Concentration of upper fluid inside fingers	0–7%	Linear relation between the camera digital level and fluorescent dye concentration
Time required to grow a PBL with excess density ≥ 0.15 kg m^{-3} t_i	54–4 s	Combination of measurements of the particle concentration measurements with estimations of the fluid phase density
Particle mass flux 20 cm below the barrier	0.21–2.60 g m^{-2} s^{-1}	Integration of the particle concentration profile at different times

The ranges of values are given by the difference between measurements performed at different particle concentrations.

Analytical Procedure

For PLIF experiments (A11–12), we calculate the local concentration of upper fluid X_f that corresponds to the proportion of upper layer fluid (containing the fluorescent dye) within the fluid phase as $X_f = D/D_u$, with D the local dye concentration and D_u the initial R6G concentration of the upper layer. We then determine the fluid density ρ_f from the concentration of upper fluid as

$$\rho_f = X_f \rho_w + \left(1 - X_f\right)\rho_s \,, \tag{10}$$

where ρ_w is the density of fresh water (that initially forms the fluid phase of the upper layer) and ρ_s is the density of the sugar solution in the lower layer. Moreover, PLIF experiments provide reproducible results, with fluid density profiles very similar from one experiment to another. This allows us to reasonably combine the fluid phase density with the particle concentration, obtained in experiments A1–10, in order to calculate the bulk mixture density ρ_m as

$$\rho_m = X_p \rho_p + \left(1 - X_p\right)\rho_f \,, \tag{11}$$

with ρ_p the particle density and $X_p = C/\rho_p$ the particle volume fraction calculated from the measured particle concentration C. At the density interface, the reduced gravity is estimated as a function of ρ_m and ρ_s as

$$g' = g\frac{\rho_m - \rho_s}{\rho_s}. \tag{12}$$

For the PBL of density ρ, the reduced gravity is calculated as $g' = g\,(\rho - \rho_s)/\rho_s$.

Whilst PLIF experiments used to infer the fluid phase density involve only small particle concentrations of 1 and 2 g l^{-1}, we additionally calculate the bulk density in experiments involving higher particle concentrations by estimating the fluid phase density from C_u = 2 g l^{-1} PLIF experiments. To do so, we assume that the spatial distribution of the fluid phase is only weakly affected by the particle concentration. Given that the particle concentration can reach up to 10 g l^{-1}, this is a strong assumption that we can only test for C_u = 1 and 2 g l^{-1} PLIF experiments for which fluid phase density profiles are indeed very similar (**Supplementary Figure S2**).

Type A particle-imaging experiments (A1–10) are processed in order to quantify the effect of particle concentration on the dynamic and geometric properties of fingers. The finger velocity is obtained by manually tracking the front position (i.e., lowest position of the interface between the finger and the lower layer fluid) over time. We measure the PBL thickness throughout experiments using both visual observations and particle concentration profiles. At the lower boundary of the PBL there is an abrupt change in particle concentration that corresponds to the transition from the particle suspension to the particle-free lower layer. We therefore define the PBL base as the position where the vertical gradient of the particle concentration reaches its minimum value. Results show that the position of the lower PBL boundary (and therefore the PBL thickness) reaches a constant height after 10 to 20 s (**Supplementary Figure S5**), when the initial effect of barrier removal disappears. The PBL thickness is finally defined as the vertical separation between the initial density interface, represented by the barrier, and the lower PBL boundary (**Figure 5**). When fingers develop, they form distinct particle-rich columns that descend into the lower layer and are characterised by bright regions in the experiments. Along a horizontal transect crossed by fingers, the light intensity profile has a peak at each finger location (**Supplementary Figure S6**). We therefore determine the number of fingers by counting the most prominent peaks along a transect located 4 cm under the upper layer, where fingers are clearly developed. This counting procedure is sensitive to detection parameters such as the vertical position of the transect or threshold values for peak prominence, width, and separation. Therefore, in order to obtain repeatable results comparable to other studies, these parameters have been selected to reproduce manual finger detection (Scollo et al., 2017) within ±1 finger. In contrast to previous methods, this allows us to quantify the temporal evolution of the number of fingers throughout the experiment duration. We assess the finger spacing λ and

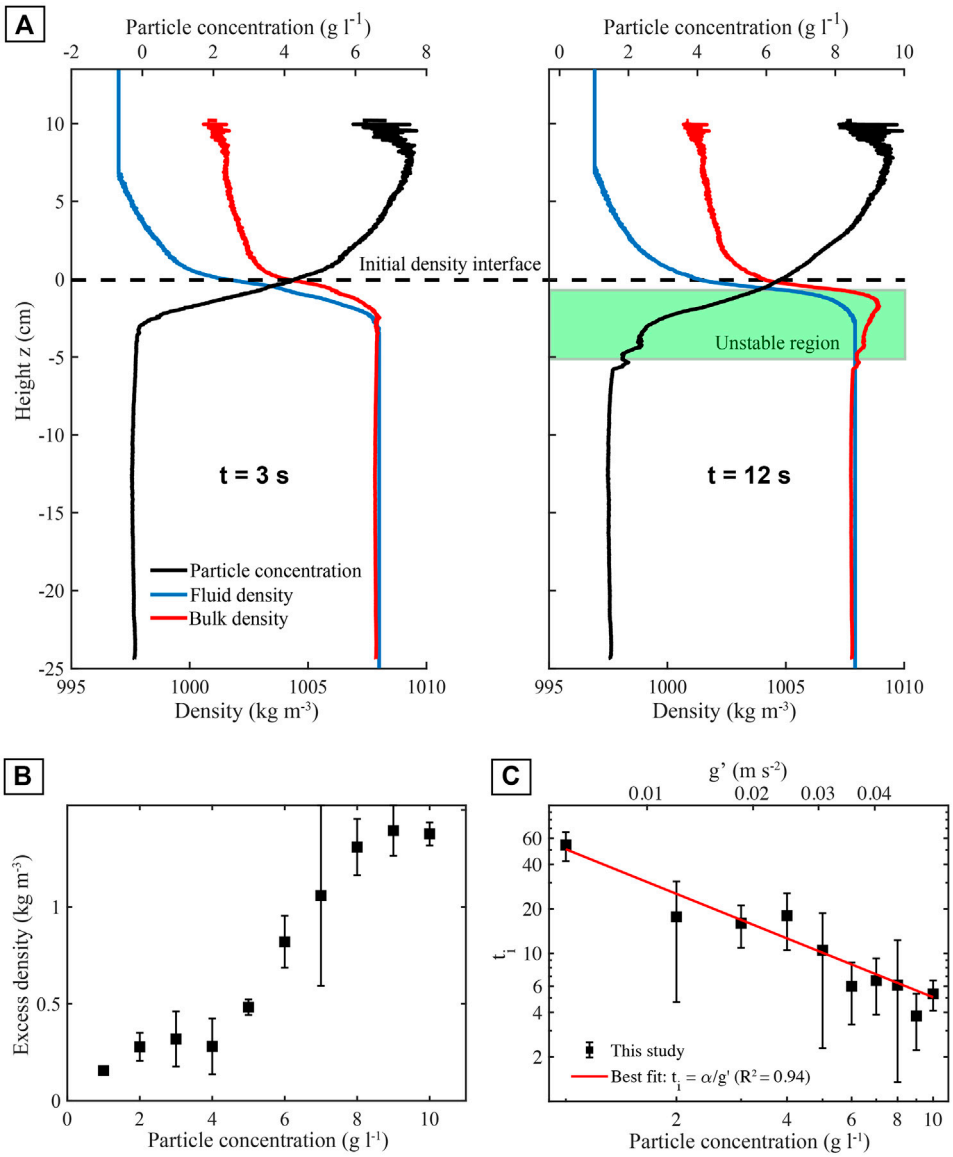

FIGURE 6 | (A) Horizontally-averaged density and particle concentration profiles for experiment A8 (initial particle concentration is 8 g l^{-1}; **Table 2**), with the fluid phase density in blue, the particle concentration in black (axis above) and the bulk mixture density in red. The initial barrier position is represented by the dashed lines. Initially, at t = 3 s **(left panel)**, the bulk stratification is stable. After some time t = 12 s **(right panel)**, the PBL develops below the interface and leads to the formation of a dense unstable region highlighted in green. For clarity, the uncertainties associated with measurements of the fluid density (corresponding to 0.8 kg m^{-3} below the density interface) are not displayed on the figures. **(B)** Variation in the excess density with particle concentration for experiments A1–A10 (**Table 2**). The particle concentration on the horizontal axis refers to the initial particle concentration of the upper layer, whereas the excess density is the maximum value for a given experiment. **(C)** Effect of particle concentration on the duration t_i required to attain an excess density ≥ 0.15 kg m^{-3} in the upper layer. Error bars correspond to the standard deviation associated with each particle concentration.

width W from visual observations (**Figure 5**). These geometrical parameters are measured 10 to 20 s after the experimental onset and at the same time as the PBL thickness, when the effect of barrier removal becomes small. λ corresponds to the distance separating two fingers and is measured at the base of the PBL, whilst W is measured at the head of the fingers (i.e., their thickest point). The uncertainty is quantified by the standard deviation from measurements of multiple fingers in each experiment. Key experimental measurements are summarised in **Table 3**.

Type B experiments are exclusively used to determine the presence or absence of fingers over a wider range of initial conditions than type A experiments. The presence of fingers is determined by visual identification of i) downward-moving particle-laden plumes, with columnar or bulbous shapes, that form at the initial density interface and inside which particles

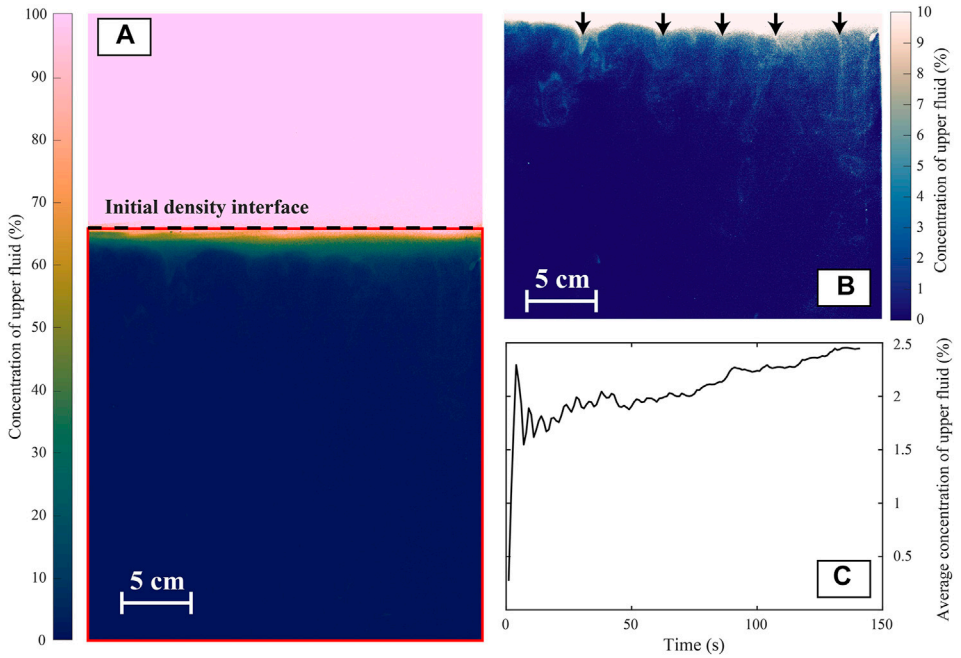

FIGURE 7 | (A) Spatial distribution of upper fluid concentration 30 s after barrier removal in experiment A11 (1 g l^{-1}). The black dashed line indicates the position of the initial density interface and the red rectangle the portion of the experiment considered to be the lower layer. **(B)** Concentration of upper fluid in the lower partition of the tank with an adjusted colormap to highlight regions of upper fluid entrainment within fingers. Black arrows show the location of leaks. **(C)** Average concentration of upper fluid in the lower layer. Oscillations in the signal at the beginning of the experiment are initially due to the removal of the barrier and then PBL detachment (see **Supplementary Video S4**). The uncertainty on the measurement is estimated to be 17%.

move faster than individually and ii) the tendency of fingers to initiate and maintain layer-scale convection in the lower partition of the tank (Hoyal et al., 1999b). We do not measure the evolution of particle concentration in type B experiments, for which the calibration presented in *Particle Imaging*. does not apply because of the low initial particle concentrations employed.

RESULTS

Evolution of Particle Concentration and Mixture Density With Time: The Formation of the PBL

Particles are initially contained in the upper part of the tank and they start sedimenting through the initial density interface after barrier removal. Subsequently, the average particle concentration decreases over time in the upper layer whilst it increases in the lower layer. In all experiments, we observe that the particle concentration in the PBL does not exceed that of the upper layer. Horizontally averaging the particle concentration at each time, we obtain particle concentration profiles for experiments A1–10. Particle concentration profiles are then combined with fluid phase density profiles (**Eq. 10**) to approximate the bulk mixture density profile (**Eq. 11**).

Figure 6A shows the evolution of bulk mixture density with time for experiment A8 (8 g l^{-1}; **Table 2**), chosen as an example since the relatively high particle concentration leads to a pronounced unstable density profile. Just after barrier removal (t = 3 s), the bulk density increases with depth in the experimental apparatus and the density profile is stable. However, particles sink below the interface and mix with the dense lower layer fluid. Consequently, an unstable heavy region associated with the PBL grows in thickness and density below the upper layer because of the added particle concentration. For experiment A8, this layer is particularly pronounced after the time t = 12 s, where it exceeds the density of the lower layer by about 1.3 kg m^{-3}.

An initial increase in density in the region immediately below the initial interface is observed in all experiments. **Figure 6B** shows the maximum excess density (i.e., difference between the density of the unstable region and that of the lower layer) vs. initial upper layer particle concentration, for experiments A1–A10 (**Table 2**). The maximum excess density gradually increases from 0.15 kg m^{-3} for a particle concentration of 1 g l^{-1} to 1.4 g m^{-3} for a particle concentration of 10 g l^{-1}.

The perturbation to the system caused by the barrier removal at the experiment onset prevents us identifying the timescale of growth of the PBL thickness, which is expected to be δ/V_p (Martin and Nokes, 1989). Because of this experimental limitation, we therefore quantify the timescale at which the density increases in

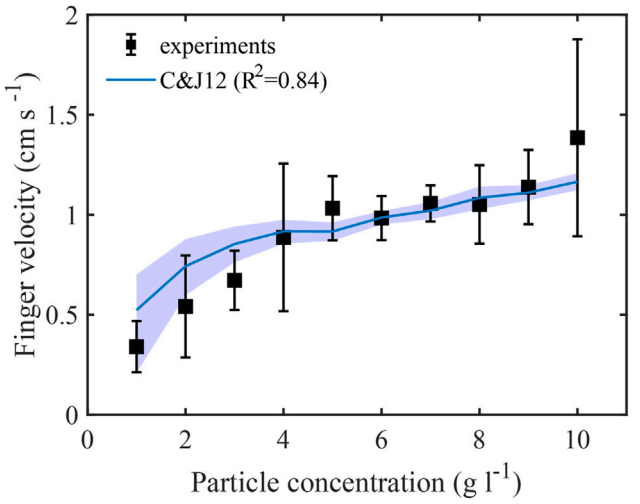

FIGURE 8 | Finger velocity as a function of initial particle concentration. The blue line corresponds to the finger velocity calculated using **Eq 13**; Hoyal et al., 1999b; Carazzo and Jellinek 2012) in combination with **Eq. 12** to obtain the reduced gravity of the PBL. The blue region corresponds to finger velocities calculated with upper fluid concentrations ranging from 0 (upper limit) to 7% (lower limit). Vertical error bars correspond to the standard deviation of the finger velocity measured in different experiments.

the PBL by measuring t_i, the time to develop an unstable layer with excess density ≥0.15 kg m^{-3}. We find that t_i decreases with C (**Supplementary Figure S7**; **Supplementary Videos S2, S3**), with t_i = 40–60 s at C_u = 1 g l^{-1} and t_i = 4–6 s at C_u = 10 g l^{-1} (**Figure 6C**). Measurements are well fitted by the relation $t_i = (\alpha/g')$, where α = 0.2 m s^{-1} is an empirically-fitted constant, dimensionally homogeneous to velocity. By analogy with the expected timescale of PBL growth, we presume that the constant α, which governs the increase of the density inside the PBL, is inversely proportional to the individual settling speed of particles.

Fluid Mixing Driven by Gravitational Instabilities and Entrainment Within Fingers

Unlike particles, the upper layer fluid phase is not significantly entrained inside the lower layer after barrier removal and fluid mixing between the upper and the lower layer is limited in proportion and vertical extent (**Figure 7**). However, we notice the development of a thin 2–3 cm mixing zone below the interface with intermediate concentrations of upper fluid (10–60%). This zone is affected by disturbances created by the initial barrier removal. Below this zone, the spatial distribution of the concentration of upper fluid shows that only small amounts of upper fluid are entrained within fingers. This entrained fluid appears as thin leaks of upper fluid [similar to those observed by Parsons et al. (2001)] with concentrations of upper fluid up to 6–7% (**Figure 7B**). Once entrained downward, portions of the upper layer are seen to buoyantly rise back up once fingers reach the bottom of the tank (**Supplementary Videos S4, S5**). On average, the concentration of upper fluid in the lower layer increases with time but remains low (<3%) (**Figure 7C**). There is an initially rapid increase at the start of the experiment due to the removal of the barrier. This is then followed by small oscillations that are linked with the thickening and retraction of the PBL at the location where fingers are formed. This thickening induces a perturbation of the lower density interface that results in an increase of the average concentration of upper fluid. The PBL later retracts to its initial position after detachment of the fingers, resulting in a decrease in the average concentration of upper fluid.

Effect of Particle Concentration on Finger Velocity, Number and Temporal Evolution

The average finger velocity increases with particle concentration (**Figure 8**), from 0.35 cm s^{-1} at C_u = 1 g l^{-1} to 1.4 cm s^{-1} for C_u = 10 g l^{-1}. We calculate the predicted characteristic finger velocity by combining the buoyancy and mass fluxes to obtain dimensions of velocity, as well as assuming that fingers have a circular cross section (Hoyal et al., 1999b; Carazzo and Jellinek, 2012)

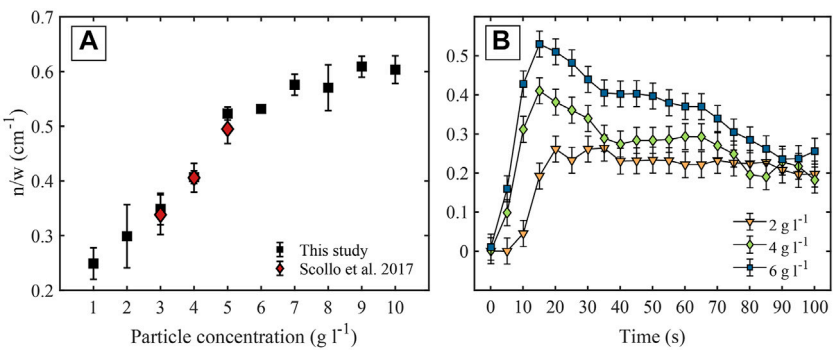

FIGURE 9 | (A) Variation in the number of fingers per unit length (*n*/*w*) as a function of particle concentration, with *n* the number of fingers and *w* the width of the experimental tank [*w* = 30.1 cm in this study and *w* = 30.3 cm for Scollo et al. (2017)]. Vertical error bars correspond to the standard deviation of the number of fingers measured in different experiments. **(B)** Evolution of the number of fingers per unit length as a function of time for selected particle concentrations. The uncertainty of 0.03 fingers cm^{-1} comes from the typical discrepancy of ± 1 fingers determined by comparing the automatic detection of fingers with visual observations.

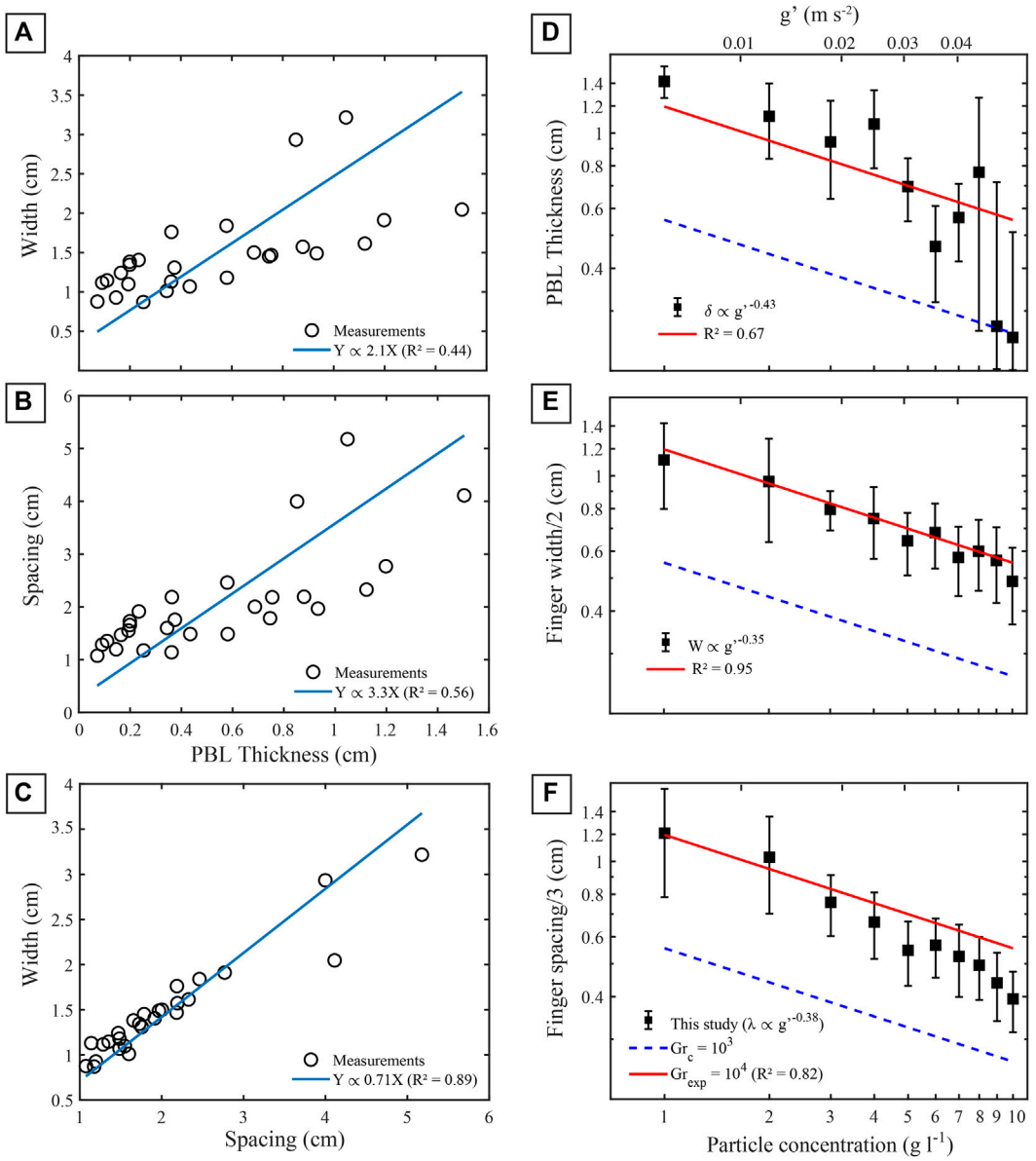

FIGURE 10 | Comparison between fingers characteristic lengths for individual experiments. **(A)** Width (W) as a function of PBL thickness (δ). **(B)** Spacing (λ) against PBL thickness **(C)** Width against spacing. The blue lines show the proportionality relationships inferred between characteristic lengths: $W = 2.1\delta$; $\lambda = 3.3\delta$; $W = 0.71\lambda$. (**D–F**) Log-log plot of the characteristic length scales of the instabilities, measured 10 to 20 s after the beginning of the experiment, including **(D)** PBL thickness δ, **(E)** finger width W and **(F)** finger spacing λ, as functions of initial particle concentration, compared to the prediction of Hoyal et al. (1999b). The blue dashed line corresponds to $Gr_c = 10^3$ and the red solid line to $Gr_{exp} = 10^4$. Vertical error bars correspond to the standard deviation of the sizes measured in different experiments.

$$V_f = g'^{\frac{2}{5}}\left(\frac{\pi V_p \delta^2}{4}\right)^{\frac{1}{5}}, \tag{13}$$

where V_p is given by **Eq. 4** and g' is calculated using **Eq. 12** and a maximum concentration of upper fluid in fingers of 7% (**Figure 8**). The characteristic length of the instability δ is measured experimentally and estimated from volume conservation to be half the finger width, which is the length scale controlling finger dynamics (Hoyal et al., 1999b). The calculated evolution of finger velocity with initial particle concentration is in good agreement with the observed finger speed ($R^2 = 0.84$).

The evolution of the maximum number of fingers per unit width as a function of both particle concentration and time has been investigated (**Figure 9**). The number of fingers increases with particle concentration, with 0.25 fingers per cm formed on average at $C_u = 1\ \mathrm{g\,l^{-1}}$ and 0.6 fingers per cm at $C_u = 10\ \mathrm{g\,l^{-1}}$. This new set of experiments agrees very well with the previous finding for the number of fingers (Scollo et al., 2017), while also expanding the previously-investigated concentration range

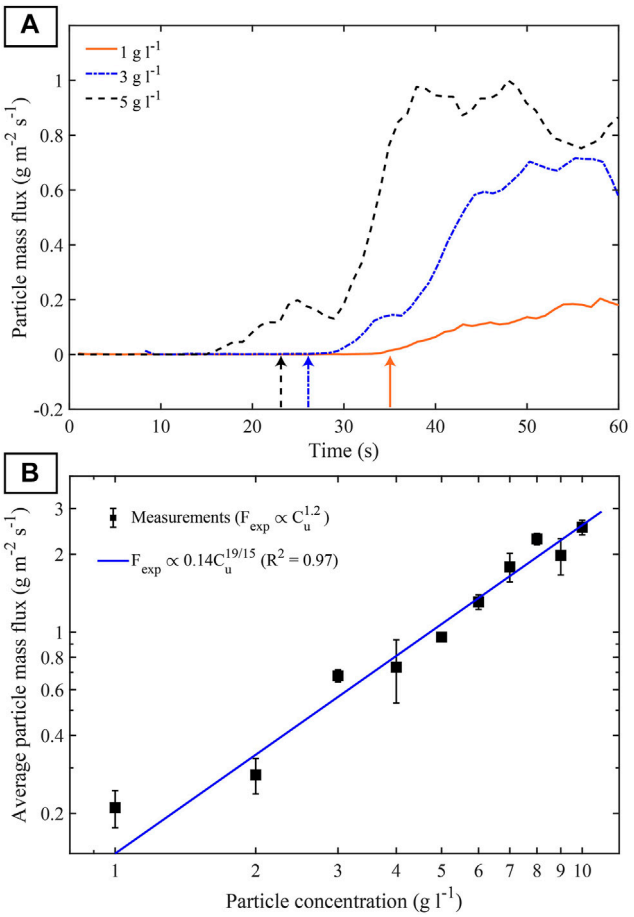

FIGURE 11 | (A) Particle mass flux F_{exp} measured in experiments 20 cm below the upper layer from **Eq. 15** for experiments A1, A3 and A6 (1, 3 and 6 g l^{-1}). The black, blue and orange arrows indicate the time l/V_f at which fingers are expected to arrive at depth l for initial particle concentrations C_u of 1, 3 and 6 g l^{-1}, respectively. Note that individually settling particles arrive at a depth 20 cm below the upper layer after a time t = 143 s that is beyond the limit of the horizontal axis **(B)** Variation in F_{exp} (averaged during 15 s after reaching a plateau value) with C_u in a log-log plot. The solid blue line shows the best fit between F_{exp} and C_u. Vertical error bars correspond to the standard deviation of the averaged particle mass flux measured in different experiments.

(**Figure 9A**). We observe the occurrence of fingers from a few seconds after barrier removal. The maximum number of fingers is achieved 10 to 20 s after barrier removal and this timing weakly depends on the particle concentration (**Figure 9B**). For high particle concentrations, the number of fingers increases at a faster rate, reaching its maximum value quicker than for low particle concentrations. For example, whilst the number of fingers increases from 0 to a maximum of 0.53 fingers per cm in 10 s for C_u = 6 g l^{-1}, it takes 20 s to achieve the maximum number of fingers of 0.27 fingers per cm for C_u = 2 g l^{-1}. The number of fingers per unit length gradually decreases after reaching its maximum value (Scollo et al., 2017) and attains a nearly constant value of approximately 0.2–0.3 cm^{-1}, regardless of the initial particle concentration. This value is possibly related to the progressive depletion of particles from the upper layer and to the merging of fingers.

Finger Length Scales in Experiments: PBL Thickness, Finger Width and Finger Spacing

As expected for such settling-driven gravitational instabilities (Hoyal et al., 1999b; Carazzo and Jellinek, 2012), all characteristic length scales, which we measure 10 to 20 s after removing the barrier, are related to each other by a proportionality coefficient. We find finger width and spacing to scale as approximately two and three times the thickness of the PBL, respectively ($W \approx 2\delta$ and $\lambda \approx 3\delta$; **Figures 10A–C**) and that all these length scales decrease with the initial particle concentration (**Figures 10D,E**). From the definition of the Grashof number (**Eq. 1**), the PBL thickness is expected to scale as (Hoyal et al., 1999b; Carazzo and Jellinek, 2012)

$$\delta = \left(\frac{Gr\,\nu^2}{g'}\right)^{\frac{1}{3}}. \tag{14}$$

Finger width and spacing should, therefore, scale similarly. Taking $Gr = Gr_c = 10^3$ provides an estimate of the critical PBL thickness (Turner, 1973; Hoyal et al., 1999b) above which convection can start (i.e., the minimum PBL thickness). This assumption, however, is found to underestimate the thickness of the PBL measured in experiments. It is therefore probable that the PBL continues to grow beyond this critical thickness. We find that a value $Gr = Gr_{exp} = 10^4$ provides a better fit between observations and **Eq. 14**. The agreement between the measurements and the model is good for the finger width and spacing, whilst **Eq. 14** predicts the thickness of the PBL

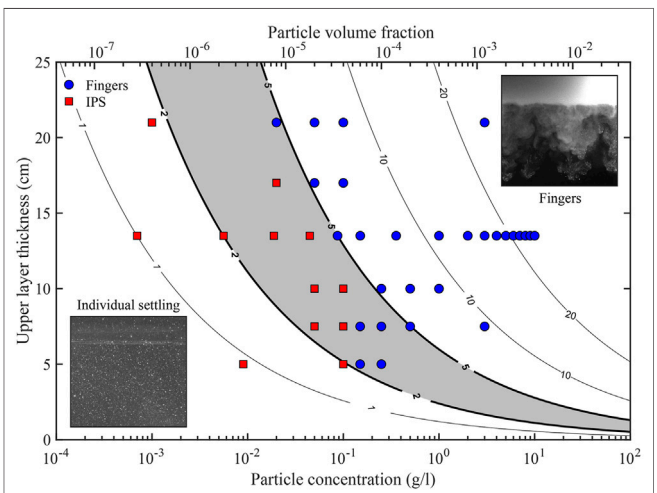

FIGURE 12 | – Contours of $L^* = H_c/\delta$ (**Eq. 16**) calculated for experiments as a function of the upper layer thickness and initial particle concentration. Calculation of L^* is performed with $Gr = Gr_{exp} = 10^4$. Blue circles and red squares correspond to experiments associated with fingers or individual particle settling (IPS), respectively (**Table 2**). The gray area $2 < L^* < 5$ indicates the transition between experiments with fingers and individual particle settling.

with less accuracy (**Figure 10**), which is characterised by more scattered data points due to the effect of barrier removal. Moreover, if we fit the measured characteristic length scales to scale with g'^m, we find $m = -0.43$ for the PBL thickness, for which the agreement with **Eq. 14** is the lowest, whereas for the finger spacing and width, $m = -0.38$ and -0.35, which are closer to the predicted value of $-1/3$.

Temporal Evolution of the Particle Mass Flux

The particle mass flux through a horizontal plane at depth l located below the upper layer can be calculated in the experiments as

$$F_{exp} = \frac{\Delta m}{A\Delta t}, \tag{15}$$

with $\Delta m = m_{t+\Delta t} - m_t$ the particle mass difference in the region below l measured in a time interval $\Delta t = 0.1$ s, and $A = 7.5 \times 30.1$ cm^2 the horizontal cross sectional area of the experimental domain. At any time, the mass of particles below l can be calculated by integrating the particle concentration profile (**Figure 6**) from the bottom of the tank $z = b$ ($z = 0$ corresponds to the height of the initial density interface) to $z = l$; $m_t = A\int_l^b C(z)dz$. This estimation of the mass does not account for the mass of particles accumulated at the bottom of the experimental tank and therefore only provides a lower limit on the particle mass flux.

Predicting the evolution of the particle mass flux in the presence of fingers is complex because a complete description requires: i) information on the 3D evolution of the finger velocity and size with time and depth, ii) a good knowledge of the duration necessary to produce fingers, and iii) a description of the particle distribution and velocity field inside fingers. It is nonetheless possible to assess the time at which the particle mass flux is expected to increase (i.e., the time at which first particles reach a depth l). Assuming that particles are coupled with the flow within fingers that form instantaneously at the start of the experiment, first particles can reach a depth l after a time l/V_f, with V_f the vertical velocity of fingers given by **Eq. 13**. In contrast, first particles settling individually from the base of the upper layer at their Stokes velocity (**Eq. 4**) are expected to reach l after a time l/V_p.

Figure 11A shows the temporal evolution of F_{exp} measured at a depth $l = 20$ cm for $C_u = 1$, 3 and 5 g l^{-1}. Generally, experiments with high particle concentrations result in larger particle mass fluxes that start to increase quicker than in experiments at lower particle concentrations. For all particle concentrations, F_{exp} increases progressively from when fingers first arrive, before reaching a more stable plateau. The particle mass flux starts to increase close to the time l/V_f (15–35 s), which is the expected arrival time for fingers, and much earlier than the expected arrival time of individual particles (143 s). F_{exp} continues to increase as more fingers reach $z = l$ and fingers become bigger through merging and entrainment of ambient fluid. The latter behavior where F_{exp} fluctuates around a plateau that occurs once the number of fingers has stabilised (**Figure 9B**) and overturning has begun in the lower layer, homogenising the particle concentration. To compare different experiments, we average F_{exp} for 15 s after the plateau is attained and plot this value as a function of C_u (**Figure 11B**). We find that the particle mass flux increases with the initial particle concentration and that a power-law with a fitted exponent of 1.2 can be used to describe the relation between F_{exp} and C_u. In particular, we note that this exponent is independent of l and varies within the interval 1.2 ± 0.1. Theoretically, we can expect $F_{exp} \propto V_f C_u$. From **Eqs 13**, **14**, the finger velocity scales with $C_u^{4/15}$ so we therefore expect the particle mass flux to be proportional to $C_u^{19/15}$. The value of the exponent $19/15 \approx 1.27$ is close to the exponent of the power-law used to fit the evolution of F_{exp} with C_u in experiments and there is a good agreement between experimental measurements and the proportionality relation $F_{exp} \propto 0.14 C_u^{19/15}$.

Potential to Form Settling-Driven Gravitational Instabilities

The tendency for settling-driven gravitational instabilities to develop below particle suspensions and to generate fingers has previously been shown to depend on the particle size. Carazzo and Jellinek (2012) compared the instability growth rate with the terminal fall velocity of individual particles and showed that fine ash promotes finger formation, whereas Scollo et al. (2017) experimentally demonstrated that coarse particle (>125 μm) settled individually in water. When particles are sufficiently small, settling-driven gravitational instabilities can form below a particle-laden layer if the time scale of particle delivery to the PBL, given by H_c/V_p, with H_c the thickness of the particle-laden layer, is greater than the time necessary to grow an unstable PBL, given by δ/V_p. This condition is independent of the particle size (i.e., V_p). Assuming that the particle concentration is homogeneous in the particle-laden layer, and that its thickness remains constant and uniform, we can therefore assess the potential for instabilities to form by evaluating the dimensionless quantity

$$L^* = \frac{H_c}{\delta}. \tag{16}$$

Combining **Eqs. 12**, **14**, **16**, L^* can be expressed as

$$L^* = H_c\left(\frac{gX_p(\rho_p - \rho_a)}{\rho_a Gr\nu^2}\right)^{\frac{1}{3}}. \tag{17}$$

$L^* >> 1$ guarantees that the PBL can reach its characteristic thickness and that fingers can possibly develop. Conversely, $L^* << 1$ means that the particle-laden layer is substantially thinner than the critical PBL thickness, thus preventing finger formation. In our experiments, we consider $H_c = H_1$, $Gr = Gr_{exp} = 10^4$ and L^* consequently ranges from 11.3 to 24.3 in type A experiments, which all produced fingers (**Table 2**). In order to better constrain the conditions leading to the formation of fingers, we explore a wider range of initial particle concentration and upper layer

thickness in type B experiments for which L^* varies from 0.8 to 25.

Figure 12 shows a regime diagram for experimental fingers as a function of upper layer thickness and initial particle concentration. Whilst fingers are observed in all the experiments performed at $L^* \geq 5$, experiments with $L^* \leq 2$ are characterised by individual particle settling and the absence of fingers (**Supplementary Video S5**). The domain defined by $2 < L^* < 5$ corresponds to a transition regime where fingers are either present or absent, depending mainly on the particle concentration, with higher particle concentrations favoring finger formation and their development, since they are more numerous and descending faster. We note that, as expected for settling-driven gravitational instabilities, high particle concentrations and thick upper layers favor the formation of fingers (Jacobs et al., 2015).

DISCUSSION

Summary of the Experimental Results and Comparison With Previous Studies

The combination of PLIF and particle imaging techniques in separate reproducible experiments provides an approximation of the bulk mixture density evolution with time. We report the formation of an unstable region in all type A experiments, which is more pronounced for high particle concentrations (**Figure 6**). From experimental observations of the evolution of the particle concentration and of the fluid and bulk mixture density, we summarise the mechanism leading to the onset of settling-driven gravitational instabilities as:

1. The initial density configuration is gravitationally stable, with a light particle-laden layer emplaced above a denser layer;
2. Particles settle across the interface from the upper layer and are incorporated in the dense lower layer fluid;
3. A thin region containing both particles and dense lower layer fluid grows below the original interface. This PBL becomes heavier than the underlying fluid because of the effect of added particles on the density of the lower layer fluid;
4. Settling-driven gravitational instabilities can occur when the thickness and density of the PBL increases causing its Gr to exceed $Gr_{exp} = 10^4$, initiating convection and resulting in the formation of fingers.

This mechanism is consistent with theoretical scenarios describing the formation and the destabilisation of a dense particle-laden layer due to particle settling as illustrated in **Figure 1** (i.e., the growing of the "nose region"; Burns and Meiburg, 2012; Burns and Meiburg, 2015; Yu et al., 2013; Davarpanah Jazi and Wells, 2020). It is worth mentioning that such a formation mechanism does not require the particle concentration inside the PBL to be greater than the initial particle concentration in the upper layer. The increase in bulk density inside the PBL is due to particles settling across the interface into the upper part of the dense lower layer that therefore becomes heavier than the fluid below. This is in agreement with our experiments where we do not observe an increase of the particle concentration inside the PBL within the uncertainty of our measurements (**Figure 6**; **Table 3**). The fact that we do not observe an increase of the particle concentration across the interface is due to the lower layer being at most 1% denser than the upper layer. Thus, in contrast with configurations involving large density differences (Carey, 1997; Manville and Wilson, 2004), particles are not significantly slowed at the interface by this density contrast and do not accumulate. Similarly, the density gradient created at the base of the upper layer (**Figure 6A**) because of barrier removal only causes negligible variations in the particle settling velocity and does not result in an increase of the particle concentration as reported by Blanchette and Bush (2005) for configurations with significant settling velocity variations.

Furthermore, our experiments suggest that fingers do not inject significant amounts of upper layer fluid into the lower layer and have an average concentration of upper fluid < 3% (**Figure 7**). This observation indicates that settling-driven gravitational instabilities only weakly affect the transport of fluid phases from the upper to the lower layer, although we observe discrete fluid leaks with concentration of upper fluid up to 7% injected through fingers propagating from the base of the upper layer (**Table 3**). The small upper fluid concentrations inside fingers suggest that their density, and hence their velocity, depends only weakly on the upper layer fluid density and is mainly controlled by the density of the lower layer fluid and the particle concentration inside fingers.

As in previous studies, we find that, along with particle size, particle concentration exerts a primary control on particle sedimentation and the formation of fingers (Del Bello et al., 2017; Scollo et al., 2017). Our results are in very good agreement with previous measurements of the number of fingers (**Figure 9**; Scollo et al., 2017) and with theoretical estimates of the finger velocity (**Figure 8**) and characteristic lengths (**Figure 10**; Hoyal et al., 1999b; Carazzo and Jellinek, 2012). This increases the confidence in these theoretical formulations of finger geometry and speed on an extended particle concentration range. However, we underline that the scaling relationships of **Eqs. 13**, **14** are not complete solutions describing the complex flow mechanisms taking place in settling-driven gravitational instabilities. They are based on simplifying assumptions regarding the choice of a single length scale characterising finger dynamics. Moreover, they do not account for the complex particle-fluid and particle-particle interactions happening inside fingers and can therefore give only first order estimates of the size and velocity of both experimental and natural fingers.

We find that the critical thickness determined with Gr_c underestimates the observed PBL thickness (**Figure 10D**) and we report that the dimensions of the instabilities formed at different particle concentrations are consistent with a value of $Gr_{exp} = 10^4$. This can be interpreted as evidence that the PBL continues to grow even after it reaches its critical thickness ($Gr = Gr_c$). Alternatively, this may also indicate that the effective PBL thickness is affected by barrier removal that initially modifies the flux of particles crossing the density interface by creating small scale eddies that quickly entrain

particles below the interface. Even if we assess the dimensions and velocity of the fingers when the effects of the initial perturbation dissipate, this experimental issue can cause differences between the measured PBL thickness and the critical thickness which would develop in an ideal case. Hence, to predict the effective instability dimensions, one should first evaluate Gr from observations of the instabilities' characteristic lengths before using **Eq. 14** to extrapolate the dimensions of the instability at different particle concentrations (i.e., different values of the reduced gravity).

Nature and Size of Volcanic ash Fingers

We find the convective scaling law of Hoyal et al. (1999b), that works well for experiments, to greatly underestimate the dimensions of volcanic ash fingers by several orders of magnitude. For example, Manzella et al. (2015) estimated the width of ash fingers at Eyjafjallajökull 2010 to be about 170 m from visual observations. Based on observations of the fingers downward velocity, they also estimated the fine ash volume fraction to be in the range of 1×10^{-6} to 4×10^{-6} and the PBL bulk density to be approximately 1.31 kg m^{-3}. Using the values of the air kinematic viscosity $\upsilon = 3 \times 10^{-5}$ m^2 s^{-1}, air density $\rho_a = 1.30$ kg m^{-3} and the Grashof number associated with experiments $Gr_{exp} = 10^4$, **Eq. 14** only yields a finger width of a few centimetres when applied to the volcanic cloud of Eyjafjallajökull. This suggests that the characterisation of the PBL in nature is highly uncertain. Therefore, this law may not be appropriate for volcanic clouds. In addition to the challenges associated with the measurements of parameters such as the fine ash concentration in volcanic clouds and the PBL, a variety of mechanisms that are not described by our experiments or by those of Hoyal et al. (1999b) and that can form fingers can also explain these discrepancies. In fact, the PBL can purely grow by particle settling, as showed in **Figures 1A,B** for our experimental configuration, and is most likely to do so in the absence of other vertical fluid motions. Evidence for this mechanisms is perhaps suggested by lidar measurements during the 1991 Mount Redoubt eruption (Hobbs et al., 1991) that showed ash fingers forming at the flat base of the volcanic cloud about 150 km from the vent ("ash veils" in their Plate 1). However, other processes present in volcanic ash clouds can also affect the sedimentation of fine ash. These include jets from overshoot regions, internal waves, overturning motions inside the cloud, and wind-driven stirring (e.g., Carazzo and Jellinek, 2012; Freret-Lorgeril et al., 2020). In addition, Mammatus clouds, i.e., formations characterised by the development of lobes on the cloud base (Schultz et al., 2006), have also been observed at the base of volcanic clouds, e.g., Mt. St. Helens, USA, 1980 (Durant et al., 2009; Carazzo and Jellinek, 2012). However, even if they share visual and dynamic similarities with settling-driven gravitational instabilities, it remains unclear if there is any link between the two phenomena.

Another source of discrepancy with the experiments is related to the fact that, unlike volcanic clouds, experiments are performed in a confined and quiescent environment, without shear at the base of the particle suspension. Although our experiments can address the case where the plume and fingers are advected at wind speed (Scollo et al., 2017), the effect of shear on the base of volcanic clouds needs to be considered in future work in order to describe more adequately the formation and the size of ash fingers. The presence of shear at the base of the cloud can affect the formation of ash fingers for two main reasons: i) shear can inhibit the formation of a PBL by producing eddies at the base the cloud that impede the sedimentation of particles across the interface and ii) it can create Kelvin-Helmoltz instabilities that will interact with settling-driven gravitational instabilities and possibly control the spatial distribution, dimensions and timing of ash fingers. Moreover, our experiments do not explore the effect of internal cloud dynamics on settling-driven gravitational instabilities. Whilst our experiments are in a transitional regime, volcanic ash clouds and ash fingers are fully turbulent and can contain vertical fluctuations that possibly affect the supply rate of particles to the PBL. We expect that more complete observations of ash fingers, combined with dedicated numerical simulations, will provide a better characterisation of ash finger sizes.

Conditions Favoring the Formation of Volcanic ash Fingers

Based on a new dimensionless number L^* (**Eqs. 16**, **17**), we assess the possibility for the PBL to grow to its characteristic thickness and therefore constrain the conditions favoring the development of fingers. We can distinguish between three regimes in experiments: i) fingers invariably form for $L^* \geq 5$ whereas, ii) they never form for $L^* \leq 2$ and iii) are either present or absent for $2 < L^* < 5$ which corresponds to a transition regime. In general, our analysis indicates that fingers are more likely to form below thick particle-laden layers associated with large particle concentrations, which correspond to $L^* \geq 5$. Calculating L^* in volcanic ash clouds is more complex and requires a good characterisation of the PBL thickness and of the eruptive parameters associated with volcanic eruptions. For instance, measurements of the fine ash concentration in volcanic clouds remain uncertain, as *in situ* characterisation of volcanic ash is often associated with the very edge of volcanic clouds due to flight restrictions of aircraft (Weber et al., 2012; Eliasson et al., 2014; Fu et al., 2015; Eliasson et al., 2016). Because of these caveats, we are not able to reliably quantify the value of L^* for natural volcanic ash clouds.

However, both the cloud thickness and the particle concentrations are related to the MER (Wilson et al., 1978; Sparks, 1986), suggesting that eruptions with high MERs are more prone to develop ash fingers (Scollo et al., 2017). Whilst L^* depends on both the particle concentration and the thickness of the upper layer (i.e., volcanic cloud), other parameters also affect the occurrence of settling-driven gravitational instabilities and the production of fingers. For example, particle size has been shown to exert a major control on the tendency to form fingers, with small particles more likely to settle collectively than coarse particles (Carazzo and Jellinek, 2012; Scollo et al., 2017). Hence, although L^* provides a good characterisation of the particle concentrations and cloud thicknesses that are associated with

fingers, it is not sufficient to obtain a complete characterisation of the conditions favoring the generation of settling-driven gravitational instabilities. L^* needs to be considered along with other parameters, such as the particle size and the cloud velocity, in order to assess the potential of volcanic ash clouds to produce fingers.

Experimental Limitations and Perspectives

As with all experimental studies, a number of limitations must be considered when interpreting the data.

First, because of the additional light scattering effect of particles, we only measure the fluid density field in PLIF experiments for low particle concentrations (1 and 2 $g\,l^{-1}$), with relatively large uncertainties ($\pm 0.8\,kg\,m^{-3}$ on average below the initial density interface). Future combined PLIF and particle imaging will allow simultaneous measurement of the particle spatial distribution and fluid density (Borg et al., 2001; Dossmann et al., 2016), thus accounting for the effect of particles on fluid density measurements. The combination of these two techniques would therefore contribute to reduce the uncertainty associated with fluid density measurements and provide estimates of the fluid phase properties for particle concentrations $>2\,g\,l^{-1}$.

Second, measurements of the PBL thickness are initially affected by a disturbance to the density interface generated when removing the barrier. We therefore measure the PBL thickness after it reaches a constant value once the initial perturbation disappears (**Supplementary Figure S5**). The initial perturbation could be reduced by using a thinner composite barrier (Dalziel, 1993; Lawrie and Dalziel, 2011) and a motorised barrier removal system (Davies Wykes and Dalziel, 2014) in order to obtain a better description of the initial growth of the PBL.

Third, the scaling of the finger size with the Grashof number works well when applied to experiments but not when applied to volcanic ash clouds. As described in *Nature and Size of Volcanic ash Fingers*, differences between the experimental configuration and volcanic clouds can explain this discrepancy, in addition to the challenges associated with the measurement of relevant parameters in natural eruption. Experiments involving particle-laden currents instead of an immobile particle suspension will contribute to better understand this discrepancy and the scaling of natural ash fingers, along with efforts in numerical simulations of the processes. In fact, the scaling analysis in *Scaling of Experiments* notably revealed that volcanic clouds are associated with a wider range of dimensionless numbers than our experiments and that *Re* and *Gr* can be orders of magnitude greater in nature (**Table 1**). This shows that volcanic clouds are much more turbulent than the analogue particle suspensions in the experiments, that are emplaced in a quiescent environment. Contrarily to the experiments, we can therefore expect turbulent motions inside the clouds to have a more pronounced effect on ash sedimentation, in particular by modulating the flux of particles entering the PBL, as described in *Nature and Size of Volcanic ash Fingers*. The discrepancy between Grashof numbers associated with the experimental and natural configuration is related to the difficulty of measuring the PBL thickness below volcanic clouds. We expect that a more complete characterisation of the parameters associated with volcanic clouds will contribute to better assess the size of the PBL and evaluate the relevance of the scaling presented in our experimental study.

Finally, laboratory experiments, unlike volcanic plumes, exist in a confined space affected by boundary conditions and the formation of return flows (Roche and Carazzo, 2019). In our experiments, boundary conditions have an impact on convection in the lower layer, which has only a limited effect on measurements of finger characteristic velocity and dimensions, especially in the early part of the experiments, and a negligible influence on finger formation. Despite these uncertainties however, we can infer useful and rigorous interpretations of the results.

CONCLUSION

Our experiments provide new insights into the development of an unstable particle-laden layer from an initially stable configuration because of particle settling across the interface. The use of PLIF has revealed that the fluid phase in the upper layer is not substantially affected by the instability and the subsequent propagation of fingers. Additionally, our experiments confirm and expand previous experimental findings and theoretical predictions concerning the increase of both finger number and speed with respect to particle concentration and the decrease of PBL and fingers size. Estimations of the particle mass flux also suggest that fingers are associated with a quicker deposition of fine particles. Finally, we propose a new dimensionless number L^* in order to assess the potential of settling-driven gravitational instabilities to occur at the base of volcanic ash clouds. In summary:

- Settling-driven gravitational instabilities in a quiescent environment arise from small density anomalies generated by particle settling across the interface and being incorporated in the denser underlying fluid (i.e., the sugar solution in experiments and the atmosphere for volcanic clouds). The bulk mixture becomes denser in this region (PBL) and destabilizes the density configuration by generating a dense layer above a lighter fluid. A gravitational instability originates and, when the PBL exceeds its critical thickness (dependent on the particle concentration), fingers begin intruding into the lower layer.
- Our new experiments validate previous results (Scollo et al., 2017) and extend them to a larger particle concentration range (from 1 to 10 $g\,l^{-1}$). Both the number of fingers and the finger velocity increase with particle concentration of the suspension, and, therefore, the importance of ash fingers on fine ash settling is expected to increase with the mass loading of ash clouds.
- Experiments show that the particle mass flux increases quicker below high particle concentration suspensions

than below particle suspensions with low particle concentrations because of the presence of fingers.
- Experimental results suggest that the characteristic lengths of the instability scale with the finger Grashof number, with $Gr_{exp} = 10^4$ in experiments. Natural ash fingers, however, may exhibit a different scaling.
- The potential to form settling-driven gravitational instabilities at the base of particle suspensions can be quantified through $L^* = H_c/\delta$ that depends on the thickness of the suspension and on the particle concentration. Our experimental results suggest that fingers form at $L^* \geq 5$ (thick upper layer and high particle concentration) and that particles settle individually at $L^* \leq 2$ (thin upper layer and low particle concentration), with a transitionary regime for $2 < L^* < 5$. Volcanic eruptions associated with large MERs as well as thick ash clouds and high particle concentrations are expected to favor the production of fingers associated with settling-driven gravitational instabilities; however, the characterization of associated PBL and ash concentrations is still too uncertain for calculating accurate values of L^*.

DATA AVAILABILITY STATEMENT

The original contributions presented in the study are included in the article/**Supplementary Material**, further inquiries can be directed to the corresponding author.

AUTHOR CONTRIBUTIONS

CB, IM, AC, and JP were involved in designing the project. AF conducted experiments and data analysis under PJ and CB supervision. AF elaborated the manuscript. All authors have contributed to data interpretation as well as the editing and finalisation of the paper.

FUNDING

The study has been funded by the Swiss National Science Foundation #200021_169463.

ACKNOWLEDGMENTS

Frédéric Arlaud and Jean-Jacques Lasserre are thanked for their technical expertise in the laboratory. We thank Mark Jellinek, TM, LM and Valerio Acocella for their comments that substantially improved the manuscript.

SUPPLEMENTARY MATERIAL

The Supplementary Material for this article can be found online at: https://www.frontiersin.org/articles/10.3389/feart.2021.640090/full#supplementary-material

REFERENCES

Adrian, R. J. (2005). Twenty Years of Particle Image Velocimetry. *Exp. Fluids* 39, 159–169. doi:10.1007/s00348-005-0991-7

Andronico, D., Scollo, S., and Cristaldi, A. (2015). Unexpected Hazards from Tephra Fallouts at Mt Etna: The 23 November 2013 Lava fountain. *J. Volcanology Geothermal Res.* 304, 118–125. doi:10.1016/j.jvolgeores.2015.08.007

Ansmann, A., Tesche, M., Groß, S., Freudenthaler, V., Seifert, P., Hiebsch, A., et al. (2010). The 16 April 2010 Major Volcanic Ash Plume over central Europe: EARLINET Lidar and AERONET Photometer Observations at Leipzig and Munich, Germany. *Geophys. Res. Lett.* 37, a–n. doi:10.1029/2010GL043809

Bagheri, G., and Bonadonna, C. (2016a). Aerodynamics of Volcanic Particles, in *Volcanic Ash* (Elsevier), 39–52. doi:10.1016/B978-0-08-100405-0.00005-7

Bagheri, G., and Bonadonna, C. (2016b). On the Drag of Freely Falling Non-spherical Particles. *Powder Tech.* 301, 526–544. doi:10.1016/j.powtec.2016.06.015

Bagheri, G., Rossi, E., Biass, S., and Bonadonna, C. (2016). Timing and Nature of Volcanic Particle Clusters Based on Field and Numerical Investigations. *J. Volcanology Geothermal Res.* 327, 520–530. doi:10.1016/j.jvolgeores.2016.09.009

Blanchette, F., and Bush, J. W. M. (2005). Particle Concentration Evolution and Sedimentation-Induced Instabilities in a Stably Stratified Environment. *Phys. Fluids* 17, 073302. doi:10.1063/1.1947987

Bonadonna, C., Mayberry, G. C., Calder, E. S., Sparks, R. S. J., Choux, C., Jackson, P., et al. (2002). Tephra Fallout in the Eruption of Soufrière Hills Volcano, Montserrat. *Geol. Soc. Lond. Mem.* 21, 483–516. doi:10.1144/GSL.MEM.2002.021.01.22

Bonadonna, C., Phillips, J. C., and Houghton, B. F. (2005). Modeling Tephra Sedimentation from a Ruapehu Weak Plume Eruption. *J. Geophys. Res.* 110, B08209. doi:10.1029/2004JB003515

Bonadonna, C., Genco, R., Gouhier, M., Pistolesi, M., Cioni, R., Alfano, F., et al. (2011). Tephra Sedimentation during the 2010 Eyjafjallajökull Eruption (Iceland) from deposit, Radar, and Satellite Observations. *J. Geophys. Res.* 116, B12202. doi:10.1029/2011JB008462

Bonadonna, C., Biass, S., Menoni, S., and Gregg, C. E. (2021). "Assessment of Risk Associated with Tephra-Related Hazards," in *Forecasting and Planning for Volcanic Hazards, Risks, and Disasters* (Elsevier), 329–378. doi:10.1016/B978-0-12-818082-2.00008-1

Borg, A., Bolinder, J., and Fuchs, L. (2001). Simultaneous Velocity and Concentration Measurements in the Near Field of a Turbulent Low-Pressure Jet by Digital Particle Image Velocimetry-Planar Laser-Induced Fluorescence. *Experiments in Fluids* 31, 140–152. doi:10.1007/s003480000267

Brown, R. J., Bonadonna, C., and Durant, A. J. (2012). A Review of Volcanic Ash Aggregation. *Phys. Chem. Earth, Parts A/B/C* 45-46, 65–78. doi:10.1016/j.pce.2011.11.001

Burgisser, A., and Bergantz, G. W. (2002). Reconciling Pyroclastic Flow and Surge: the Multiphase Physics of Pyroclastic Density Currents. *Earth Planet. Sci. Lett.* 202, 405–418. doi:10.1016/s0012-821x(02)00789-6

Burgisser, A., Bergantz, G. W., and Breidenthal, R. E. (2005). Addressing Complexity in Laboratory Experiments: the Scaling of Dilute Multiphase Flows in Magmatic Systems. *J. Volcanology Geothermal Res.* 141, 245–265. doi:10.1016/j.jvolgeores.2004.11.001

Burns, P., and Meiburg, E. (2012). Sediment-laden Fresh Water above Salt Water: Linear Stability Analysis. *J. Fluid Mech.* 691, 279–314. doi:10.1017/jfm.2011.474

Burns, P., and Meiburg, E. (2015). Sediment-laden Fresh Water above Salt Water: Nonlinear Simulations. *J. Fluid Mech.* 762, 156–195. doi:10.1017/jfm.2014.645

Carazzo, G., and Jellinek, A. M. (2012). A New View of the Dynamics, Stability and Longevity of Volcanic Clouds. *Earth Planet. Sci. Lett.* 325–326, 39–51. doi:10.1016/j.epsl.2012.01.025

Carazzo, G., and Jellinek, A. M. (2013). Particle Sedimentation and Diffusive Convection in Volcanic Ash-Clouds. *J. Geophys. Res. Solid Earth* 118, 1420–1437. doi:10.1002/jgrb.50155

Cardoso, S. S. S., and Zarrebini, M. (2001). Convection Driven by Particle Settling Surrounding a Turbulent Plume. *Chem. Eng. Sci.* 56, 3365–3375. doi:10.1016/S0009-2509(01)00028-8

Carey, S. (1997). Influence of Convective Sedimentation on the Formation of Widespread Tephra Fall Layers in the Deep Sea. *Geol* 25, 839–842. doi:10.1130/0091-7613(1997)025<0839:iocsot>2.3.co;2

Chen, C. F. (1997). Particle Flux through Sediment Fingers. *Deep Sea Res. Oceanographic Res. Pap.* 44, 1645–1654. doi:10.1016/S0967-0637(97)00042-3

Chou, Y.-J., and Shao, Y.-C. (2016). Numerical Study of Particle-Induced Rayleigh-Taylor Instability: Effects of Particle Settling and Entrainment. *Phys. Fluids* 28, 043302. doi:10.1063/1.4945652

Costa, A., Folch, A., and Macedonio, G. (2010). A Model for Wet Aggregation of Ash Particles in Volcanic Plumes and Clouds: 1. Theoretical Formulation. *J. Geophys. Res.* 115, B09201. doi:10.1029/2009JB007175

Crimaldi, J. P. (2008). Planar Laser Induced Fluorescence in Aqueous Flows. *Exp. Fluids* 44, 851–863. doi:10.1007/s00348-008-0496-2

Crowe, C. T., Schwarzkopf, J. D., Sommerfeld, M., and Tsuji, Y. (2011). *Multiphase Flows with Droplets and Particles*. 2nd Edn. CRC Press. doi:10.1201/b11103

Dalziel, S. B. (1993). Rayleigh-Taylor Instability: Experiments with Image Analysis. *Dyn. Atmospheres Oceans* 20, 127–153. doi:10.1016/0377-0265(93)90051-8

Davarpanah Jazi, S., and Wells, M. G. (2016). Enhanced Sedimentation beneath Particle-Laden Flows in Lakes and the Ocean Due to Double-Diffusive Convection. *Geophys. Res. Lett.* 43 (10), 883–910. doi:10.1002/2016GL069547

Davarpanah Jazi, S., and Wells, M. G. (2020). Dynamics of Settling Driven Convection beneath a Sediment Laden Buoyant Overflow: Implications for the Length Scale of Deposition in Lakes and the Coastal Ocean. *Sedimentology* 67, 699–720. doi:10.1111/sed.12660

Davies Wykes, M. S., and Dalziel, S. B. (2014). Efficient Mixing in Stratified Flows: Experimental Study of a Rayleigh-Taylor Unstable Interface within an Otherwise Stable Stratification. *J. Fluid Mech.* 756, 1027–1057. doi:10.1017/jfm.2014.308

Del Bello, E., Taddeucci, J., de' Michieli Vitturi, M., Scarlato, P., Andronico, D., Scollo, S., et al. (2017). Effect of Particle Volume Fraction on the Settling Velocity of Volcanic Ash Particles: Insights from Joint Experimental and Numerical Simulations. *Sci. Rep.* 7, 39620. doi:10.1038/srep39620

Dossmann, Y., Bourget, B., Brouzet, C., Dauxois, T., Joubaud, S., and Odier, P. (2016). Mixing by Internal Waves Quantified Using Combined PIV/PLIF Technique. *Exp. Fluids* 57, 132. doi:10.1007/s00348-016-2212-y

Durant, A. J., and Brown, R. J. (2016). "Ash Aggregation in Volcanic Clouds," in *Volcanic Ash* (Elsevier), 53–65. doi:10.1016/B978-0-08-100405-0.00006-9

Durant, A. J., Rose, W. I., Sarna-Wojcicki, A. M., Carey, S., and Volentik, A. C. M. (2009). Hydrometeor-enhanced Tephra Sedimentation: Constraints from the 18 May 1980 Eruption of Mount St. Helens. *J. Geophys. Res.* 114, B03204. doi:10.1029/2008JB005756

Durant, A. J. (2015). Research Focus: Toward a Realistic Formulation of fine-ash Lifetime in Volcanic Clouds. *Geology* 43, 271–272. doi:10.1130/focus032015.1

Eliasson, J., Yoshitani, J., Weber, K., Yasuda, N., Iguchi, M., and Vogel, A. (2014). Airborne Measurement in the Ash Plume from Mount Sakurajima: Analysis of Gravitational Effects on Dispersion and Fallout. *Int. J. Atmos. Sci.* 2014, 1–16. doi:10.1155/2014/372135

Eliasson, J., Watson, I. M., and Weber, K. (2016). "*In Situ* Observations of Airborne Ash from Manned Aircraft," in *Volcanic Ash* (Elsevier), 89–98. doi:10.1016/B978-0-08-100405-0.00009-4

Folch, A., Costa, A., and Macedonio, G. (2016). FPLUME-1.0: An Integral Volcanic Plume Model Accounting for Ash Aggregation. *Geosci. Model. Dev.* 9, 431–450. doi:10.5194/gmd-9-431-2016

Folch, A. (2012). A Review of Tephra Transport and Dispersal Models: Evolution, Current Status, and Future Perspectives. *J. Volcanology Geothermal Res.* 235–236, 96–115. doi:10.1016/j.jvolgeores.2012.05.020

Freret-Lorgeril, V., Gilchrist, J., Donnadieu, F., Jellinek, A. M., Delanoë, J., Latchimy, T., et al. (2020). Ash Sedimentation by Fingering and Sediment Thermals from Wind-Affected Volcanic Plumes. *Earth Planet. Sci. LettersSci. Lett.* 534, 116072. doi:10.1016/j.epsl.2020.116072

Fu, G., Lin, H. X., Heemink, A. W., Segers, A. J., Lu, S., and Palsson, T. (2015). Assimilating Aircraft-Based Measurements to Improve Forecast Accuracy of Volcanic Ash Transport. *Atmos. Environ.* 115, 170–184. doi:10.1016/j.atmosenv.2015.05.061

Gouhier, M., Eychenne, J., Azzaoui, N., Guillin, A., Deslandes, M., Poret, M., et al. (2019). Low Efficiency of Large Volcanic Eruptions in Transporting Very fine Ash into the Atmosphere. *Sci. Rep.* 9, 1449. doi:10.1038/s41598-019-38595-7

Grant, I. (1997). Particle Image Velocimetry: A Review. *Proc. Inst. Mech. Eng. Part. C J. Mech. Eng. Sci.* 211, 55–76. doi:10.1243/0954406971521665

Green, T. (1987). The Importance of Double Diffusion to the Settling of Suspended Material. *Sedimentology* 34, 319–331. doi:10.1111/j.1365-3091.1987.tb00780.x

Gudmundsson, G. (2011). Respiratory Health Effects of Volcanic Ash with Special Reference to Iceland. A Review. *Clin. Respir. J.* 5, 2–9. doi:10.1111/j.1752-699X.2010.00231.x

Guffanti, M., Mayberry, G. C., Casadevall, T. J., and Wunderman, R. (2009). Volcanic Hazards to Airports. *Nat. Hazards* 51, 287–302. doi:10.1007/s11069-008-9254-2

Harlow, F. H., and Amsden, A. A. (1975). Numerical Calculation of Multiphase Fluid Flow. *J. Comput. Phys.* 17, 19–52. doi:10.1016/0021-9991(75)90061-3

Henniger, R., and Kleiser, L. (2012). Temporal Evolution, Morphology, and Settling of the Sediment Plume in a Model Estuary. *Phys. Fluids* 24, 086601. doi:10.1063/1.4739537

Hobbs, P. V., Radke, L. F., Lyons, J. H., Ferek, R. J., Coffman, D. J., and Casadevall, T. J. (1991). Airborne Measurements of Particle and Gas Emissions from the 1990 Volcanic Eruptions of Mount Redoubt. *J. Geophys. Res.* 96, 18735. doi:10.1029/91JD01635

Horwell, C. J., and Baxter, P. J. (2006). The Respiratory Health Hazards of Volcanic Ash: a Review for Volcanic Risk Mitigation. *Bull. Volcanol.* 69, 1–24. doi:10.1007/s00445-006-0052-y

Hoyal, D. C. J. D., Bursik, M. I., and Atkinson, J. F. (1999a). The Influence of Diffusive Convection on Sedimentation from Buoyant Plumes. *Mar. Geology.* 159, 205–220. doi:10.1016/S0025-3227(99)00005-5

Hoyal, D. C. J. D., Bursik, M. I., and Atkinson, J. F. (1999b). Settling-driven Convection: A Mechanism of Sedimentation from Stratified Fluids. *J. Geophys. Res.* 104, 7953–7966. doi:10.1029/1998JC900065

Hu, H., Saga, T., Kobayashi, T., and Taniguchi, N. (2002). Simultaneous Velocity and Concentration Measurements of a Turbulent Jet Mixing Flow. *Ann. N. Y. Acad. Sci.* 972, 254–259. doi:10.1111/j.1749-6632.2002.tb04581.x

Inman, D. L. (1952). Measures for Describing the Size Distribution of Sediments. *J. Sediment. Res.* 22 (3), 125–145. doi:10.1306/D42694DB-2B26-11D7-8648000102C1865D

Jacobs, C. T., Collins, G. S., Piggott, M. D., Kramer, S. C., and Wilson, C. R. G. (2013). Multiphase Flow Modelling of Volcanic Ash Particle Settling in Water Using Adaptive Unstructured Meshes. *Geophys. J. Int.* 192, 647–665. doi:10.1093/gji/ggs059

Jacobs, C. T., Goldin, T. J., Collins, G. S., Piggott, M. D., Kramer, S. C., Melosh, H. J., et al. (2015). An Improved Quantitative Measure of the Tendency for Volcanic Ash Plumes to Form in Water: Implications for the Deposition of marine Ash Beds. *J. Volcanology Geothermal Res.* 290, 114–124. doi:10.1016/j.jvolgeores.2014.10.015

Jenkins, S. F., Wilson, T. M., Magill, C., Miller, V., Stewart, C., Blong, R., et al. (2015). "Volcanic Ash Fall hazard and Risk," in *Global Volcanic Hazards and Risk*. Editors S. C. Loughlin, S. Sparks, S. K. Brown, S. F. Jenkins, and C. Vye-Brown (Cambridge: Cambridge University Press), 173–222. doi:10.1017/CBO9781316276273.005

Kavanagh, J. L., Engwell, S. L., and Martin, S. A. (2018). A Review of Laboratory and Numerical Modelling in Volcanology. *Solid Earth* 9, 531–571. doi:10.5194/se-9-531-2018

Keane, R. D., and Adrian, R. J. (1992). Theory of Cross-Correlation Analysis of PIV Images. *Appl. Scientific Res.* 49, 191–215. doi:10.1007/BF00384623

Koochesfahani, M. M. (1984). *Experiments on Turbulent Mixing and Chemical Reactions in a Liquid Mixing Layer*. Dissertation (Ph.D). California Institute of Technology. doi:10.7907/Y7BR-C556

Lawrie, A. G. W., and Dalziel, S. B. (2011). Rayleigh-Taylor Mixing in an Otherwise Stable Stratification. *J. Fluid Mech.* 688, 507–527. doi:10.1017/jfm.2011.398

Lechner, P., Tupper, A., Guffanti, M., Loughlin, S., and Casadevall, T. (2017). "Volcanic Ash and Aviation The Challenges of Real Time, Global Communication of a Natural Hazard," in *Observing the Volcano World.*

Editors C. J. Fearnley, D. K. Bird, K. Haynes, W. J. McGuire, and G. Jolly (Cham: Springer International Publishing), 51–64. doi:10.1007/11157_2016_49

Lee, S., Jang, Y., Choi, C., and Lee, T. (1992). Combined Effect of Sedimentation Velocity Fluctuation and Self Sharpening on Interface Broadening. *Phys. Fluids A: Fluid Dyn.* 4, 2601–2606. doi:10.1063/1.858449

Linden, P. F., and Redondo, J. M. (1991). Molecular Mixing in Rayleigh-Taylor Instability. Part I: Global Mixing. *Phys. Fluids A: Fluid Dyn.* 3, 1269–1277. doi:10.1063/1.858055

Manville, V., and Wilson, C. J. N. (2004). Vertical Density Currents: a Review of Their Potential Role in the Deposition and Interpretation of Deep-Sea Ash Layers. *J. Geol. Soc.* 161, 947–958. doi:10.1144/0016-764903-067

Manzella, I., Bonadonna, C., Phillips, J. C., and Monnard, H. (2015). The Role of Gravitational Instabilities in Deposition of Volcanic Ash. *Geology* 43, 211–214. doi:10.1130/G36252.1

Marsh, B. D. (1988). Crystal Capture, Sorting, and Retention in Convecting Magma. *GSA Bull.* 100, 1720–1737. doi:10.1130/0016-7606(1988)100<1720:ccsari>2.3.co;2

Martin, D., and Nokes, R. (1989). A Fluid-Dynamical Study of Crystal Settling in Convecting Magmas. *J. Petrol.* 30, 1471–1500. doi:10.1093/petrology/30.6.1471

Martin, J., Rakotomalala, N., and Salin, D. (1994). Hydrodynamic Dispersion Broadening of a Sedimentation Front. *Phys. Fluids* 6, 3215–3217. doi:10.1063/1.868051

Maxworthy, T. (1999). The Dynamics of Sedimenting Surface Gravity Currents. *J. Fluid Mech.* 392, 27–44. doi:10.1017/S002211209900556X

Nicholas, A. P., and Walling, D. E. (1996). The Significance of Particle Aggregation in the Overbank Deposition of Suspended Sediment on River Floodplains. *J. Hydrol.* 186, 275–293. doi:10.1016/S0022-1694(96)03023-5

Parsons, J. D., Bush, J. W. M., and Syvitski, J. P. M. (2001). Hyperpycnal Plume Formation from Riverine Outflows with Small Sediment Concentrations. *Sedimentology* 48, 465–478. doi:10.1046/j.1365-3091.2001.00384.x

Prata, A. J., and Tupper, A. (2009). Aviation Hazards from Volcanoes: the State of the Science. *Nat. Hazards* 51, 239–244. doi:10.1007/s11069-009-9415-y

Reynolds, O. (1883). An Experimental Investigation of the Circumstances Which Determine whether the Motion of Water Shall Be Direct or Sinuous, and of the Law of Resistance in Parallel Channels. *Philos. Trans. R. Soc. Lond.* 174, 935–982. doi:10.1098/rstl.1883.0029

Roche, O., and Carazzo, G. (2019). The Contribution of Experimental Volcanology to the Study of the Physics of Eruptive Processes, and Related Scaling Issues: A Review. *J. Volcanology Geothermal Res.* 384, 103–150. doi:10.1016/j.jvolgeores.2019.07.011

Schultz, D. M., Kanak, K. M., Straka, J. M., Trapp, R. J., Gordon, B. A., Zrnić, D. S., et al. (2006). The Mysteries of Mammatus Clouds: Observations and Formation Mechanisms. *J. Atmos. Sci.* 63, 2409–2435. doi:10.1175/JAS3758.1

Scollo, S., Tarantola, S., Bonadonna, C., Coltelli, M., and Saltelli, A. (2008). Sensitivity Analysis and Uncertainty Estimation for Tephra Dispersal Models. *J. Geophys. Res.* 113, B06202. doi:10.1029/2006JB004864

Scollo, S., Bonadonna, C., and Manzella, I. (2017). Settling-driven Gravitational Instabilities Associated with Volcanic Clouds: New Insights from Experimental Investigations. *Bull. Volcanol.* 79. doi:10.1007/s00445-017-1124-x

Sharp, D. H. (1984). An overview of Rayleigh-Taylor instability. *Phys. Nonlinear Phenom.* 12, 3–18. doi:10.1016/0167-2789(84)90510-4

Sparks, R. S. J. (1986). The Dimensions and Dynamics of Volcanic Eruption Columns. *Bull. Volcanol.* 48, 3–15. doi:10.1007/BF01073509

Spence, R. J. S., Kelman, I., Baxter, P. J., Zuccaro, G., and Petrazzuoli, S. (2005). Residential Building and Occupant Vulnerability to Tephra Fall. *Nat. Hazards Earth Syst. Sci.* 5, 477–494. doi:10.5194/nhess-5-477-2005

Sutherland, B. R., Gingras, M. K., Knudson, C., Steverango, L., and Surma, C. (2018). Particle-bearing Currents in Uniform Density and Two-Layer Fluids. *Phys. Rev. Fluids* 3, 023801. doi:10.1103/PhysRevFluids.3.023801

Suzuki, Y. J., and Koyaguchi, T. (2009). A Three-Dimensional Numerical Simulation of Spreading Umbrella Clouds. *J. Geophys. Res.* 114, B03209. doi:10.1029/2007JB005369

Troy, C. D., and Koseff, J. R. (2005). The Generation and Quantitative Visualization of Breaking Internal Waves. *Exp. Fluids* 38, 549–562. doi:10.1007/s00348-004-0909-9

Turner, J. S. (1973). *Buoyancy Effects in Fluids*. 1st Edn. Cambridge University Press. doi:10.1017/CBO9780511608827

Valentine, G. A., and Wohletz, K. H. (1989). Numerical Models of Plinian Eruption Columns and Pyroclastic Flows. *J. Geophys. Res.* 94, 1867. doi:10.1029/JB094iB02p01867

Weber, K., Eliasson, J., Vogel, A., Fischer, C., Pohl, T., van Haren, G., et al. (2012). Airborne *In-Situ* Investigations of the Eyjafjallajökull Volcanic Ash Plume on Iceland and over north-western Germany with Light Aircrafts and Optical Particle Counters. *Atmos. Environ.* 48, 9–21. doi:10.1016/j.atmosenv.2011.10.030

Wilson, P. N., and Andrews, M. J. (2002). Spectral Measurements of Rayleigh-Taylor Mixing at Small Atwood Number. *Phys. Fluids* 14, 938–945. doi:10.1063/1.1445418

Wilson, L., Sparks, R. S. J., Huang, T. C., and Watkins, N. D. (1978). The Control of Volcanic Column Heights by Eruption Energetics and Dynamics. *J. Geophys. Res.* 83, 1829–1836. doi:10.1029/JB083iB04p01829

Wilson, T. M., Stewart, C., Sword-Daniels, V., Leonard, G. S., Johnston, D. M., Cole, J. W., et al. (2012). Volcanic Ash Impacts on Critical Infrastructure. *Phys. Chem. Earth, Parts A/B/C* 45-46, 5–23. doi:10.1016/j.pce.2011.06.006

Yu, X., Hsu, T.-J., and Balachandar, S. (2013). Convective Instability in Sedimentation: Linear Stability Analysis. *J. Geophys. Res. Oceans* 118, 256–272. doi:10.1029/2012JC008255

Yu, X., Hsu, T.-J., and Balachandar, S. (2014). Convective Instability in Sedimentation: 3-D Numerical Study. *J. Geophys. Res. Oceans* 119, 8141–8161. doi:10.1002/2014JC010123

Zehentbauer, F. M., Moretto, C., Stephen, R., Thevar, T., Gilchrist, J. R., Pokrajac, D., et al. (2014). Fluorescence Spectroscopy of Rhodamine 6G: Concentration and Solvent Effects. *Spectrochimica Acta A: Mol. Biomol. Spectrosc.* 121, 147–151. doi:10.1016/j.saa.2013.10.062

Zimmermann-Timm, H. (2002). Characteristics, Dynamics and Importance of Aggregates in Rivers - an Invited Review. *Internat. Rev. Hydrobiol.* 87, 197–240. doi:10.1002/1522-2632(200205)87:2/3<197::aid-iroh197>3.0.co;2-7

Conflict of Interest: The authors declare that the research was conducted in the absence of any commercial or financial relationships that could be construed as a potential conflict of interest.